Journal of Sound and Vibration (1998) **210**(2), 171–214

MULTI-BODY DYNAMICS AND MODAL ANALYSIS OF COMPLIANT GEAR BODIES

H. VINAYAK† AND R. SINGH

Acoustics and Dynamics Laboratory, Department of Mechanical Engineering, The Ohio State University, Columbus, OH 43210-1107, *U.S.A.*

(*Received* 24 *March* 1997, *and in final form* 8 *September* 1997)

This paper extends the multi-body dynamics modelling strategy for rigid gears to include compliant gear bodies in multi-mesh transmissions. Only external, fixed center, helical or spur gears are considered. This formulation combines distributed gear mesh stiffness and gear blank compliance models in a multi-body dynamics framework resulting in a set of non-linear differential equations with time-varying coefficients. Linearization and other simplifications are applied to yield the resulting linear time-invariant equations of motion. Several solution techniques are then used to determine eigensolutions and forced harmonic responses. The resulting normal mode solutions are compared to those obtained by the finite element analysis for several examples of transmission containing flexible gears. These include ring-gears and bodies with discontinuities. A parametric study has been performed to assess the effect of gear orientation on the dynamics of transmissions. Finally analytical predictions are compared to the results of a laboratory experiment.

1. INTRODUCTION

Multi-mesh geared systems containing thin, weight-optimized gear bodies are common in many applications including rotorcraft and automotive transmissions. The natural frequencies of such compliant gears may lie within the gear mesh frequency excitation regimes. Several noise, vibration and dynamic problems have been reported in the literature [1–4]. However, gear dynamics researchers have focused mostly on the mathematical analyses of systems with rigid gears, as evident from the literature reviews conducted by Ozguven and Houser [5] and later by Blankenship and Singh [6]. Limited studies on multi-mesh systems with rigid gears have been performed in the past including the effort by Iida *et al*. [7], Blankenship and Singh [8], Vinayak *et al*. [9], Velex and Flamand [10] and Nogill [40] among others. A new and comprehensive analysis of multi-mesh geared systems was presented by the authors [9] which included shaft and bearing deformations but only for rigid gears. Very few researchers have attempted to include the gear body elasticity together with the rigid body modes of the geared system. Amirouche [11, 12] used a combination of finite elements and multi-body dynamics formulation based on the Kane's equations [13] to develop a composite model of compliant gear and teeth. This modelling technique results in an extremely large number of d.o.f. which makes the overall problem computationally intensive. Another multi-body modelling strategy, as developed by Shabana [14–20], uses generalized displacement co-ordinates together with deformation shape function to obtain dynamic equations for multi-body systems with flexible bodies. This is especially attractive for relatively smaller multi-body systems where this formulation can be applied with moderate computational

† Currently at BFGoodrich Aerospace, Troy, OH 45373, USA.

0022–460X/98/070171 + 44 $25.00/0/sv971298

effort. Hence, this solution strategy will be followed in our analysis of transmission systems with flexible gears which typically may have only a few gears meshing together. The methodology for rigid gears has already been presented in reference [9].

A compliant gear body may exhibit both transverse (like an annular plate in flexure) and in-plane (like a ring) motions. There is a substantial body of literature on the vibration characteristics of circular plates as evident from the well-known monograph by Leissa [21]. A few researchers such as Yu and Mote [22] have included the effect of small perturbations such as thin slots on the overall dynamics of vibrating or rotating plates. An extensive study of gear-like disks with holes, slots, thick rims and hubs is presented by the authors of this article in earlier publications [23, 24]. Eigensolutions of both free–free and clamped–free disks (with impedance boundary conditions at the disk-shaft interface) have been calculated and validated in references [9, 23, 24]. Dynamic behavior of rings and ring-like structures have also been studied by a number of investigators. For instance, Lin and Soedel [25, 26] and Soedel [27] proposed deformation shape functions and governing equations for rotating thick and thin circular rings. Huang and Soedel [28–30] have discussed the effect of dynamic forces on the vibration characteristics of a ring. In particular they have also compared the response of a rotating ring with stationary force with that of a stationary ring excited by a rotating force [28].

2. SCOPE AND OBJECTIVES

It is clear from the literature that an analytical methodology that specifically addresses the dynamics of multi-mesh geared systems with compliant gears has yet to be formulated. This paper attempts to bridge this void by focusing on a comprehensive yet tractable solution technique which can be implemented for efficient and reasonably accurate analyses. Given the complexity of the problem, the scope of this paper is limited to the examination of only external, involute gears and each spur or helical gear is assumed to have a fixed center of rotation, as in reference [9]. Figure 1 illustrates four generic configurations which will be used to illustrate our methodology. As a prelude to a more complicated analysis, results of only linear time-invariant (LTI) systems are presented in order to enhance our understanding of the dynamic characteristics of the type of practical systems shown schematically in Figure 1.

Specific objectives of this paper are as follows: (1) to formulate a new dynamic gear mesh force expression for systems consisting of compliant gears; (2) to extend this mesh formulation to multi-mesh geared systems by using the multi-body dynamics (MBD) techniques which results in non-linear system equations with time or position varying coefficients (NLTV); (3) to reduce this equation to a more convenient linearized formulation with time or position varying coefficients (LTV) and finally to a tractable linear time-invariant (LTI) formulation and study the validity of this reduction; (4) to compare the dynamic characteristics of a system with compliant versus rigid gears, and in particular study the effect of force coupling between the rigid body and compliant body d.o.f.; (5) to validate the proposed methodology by comparing the resulting eigensolutions for configurations shown in Figure 1 with those predicted by the finite element method (FEM); (6) to formulate an analytical strategy to calculate forced response characteristics of a geared system with compliant gears; and (7) to validate methodology by comparing predictions with FEM results or limited measurements on a gear-like disk. Overall this article will attempt to extend prior articles [9, 23] by the same authors.

Some typical eigenvalues of a compliant gear-like disk are shown in Figure 2, as predicted by FEM. Observe that the in-plane ring modes (in radial direction) are dominant when $(r_o - r_i)/\bar{r} \ll 1{\cdot}0$ where r_o, r_i and $\bar{r}$ are the outer, inner and mean radii of a disk.

Conversely, the out-of-plane plate modes (normal to the disk surface) dominate when $(r_o - r_i)/\bar{r} \geqslant 1{\cdot}0$. These two limiting cases are analyzed and integrated in the multi-body dynamics methodology as demonstrated by Figures 3(a) and (b). For a complicated gear blank geometry with arbitrary boundary conditions like Figure 3(c), eigensolutions or shape functions can be obtained *a priori*, say from FEM. All three cases will be discussed further in section 4.

3. SINGLE MESH FORMULATION FOR COMPLIANT GEARS

3.1. GOVERNING EQUATIONS

The single gear pair mesh dynamics for systems containing rigid gears was presented in an earlier paper by the authors [9]. This formulation is extended here to include effects of flexibility of the gear blanks themselves as shown in a flowchart form in Figure 4. Like the earlier paper the equations of motion for the gear i in a pair i–j is given in the dual domain $(t, \theta^i{*})$ form as follows where t is time, $\theta^i{*} = \int_0^t \Omega^i{*}\,\mathrm{d}t$ is the mean rotational component and $\Omega^i{*}$ is the mean rotational velocity of gear i:

$$\begin{aligned}\mathbf{M}^i(\theta^i{*})\ddot{\mathbf{q}}^i_m(t) + \mathbf{C}^{ij-i}_m(\theta^i{*})\dot{\mathbf{q}}^i_m(t) - \mathbf{C}^{ij-j}_m(\theta^i{*})\dot{\mathbf{q}}^j_m(t) + \mathbf{K}^{ij-i}_m(\theta^i{*})\mathbf{q}^i_m - \mathbf{K}^{ij-j}_m(\theta^i{*})\mathbf{q}^j_m \\ + \mathbf{K}^i_{sb}(\theta^i{*})\mathbf{q}^i_m(t) + \mathbf{K}^i_{ff}(\theta^i{*})\mathbf{q}^i_m(t) \\ = \mathbf{Q}^i_{me}(t) + \mathbf{Q}^i(t) - (\mathbf{Q}^{ij-i}_{mg}{*}(\Omega{*}, t) - \mathbf{Q}^{ij-j}_{mg}{*}(\Omega{*}, t)),\end{aligned} \tag{1}$$

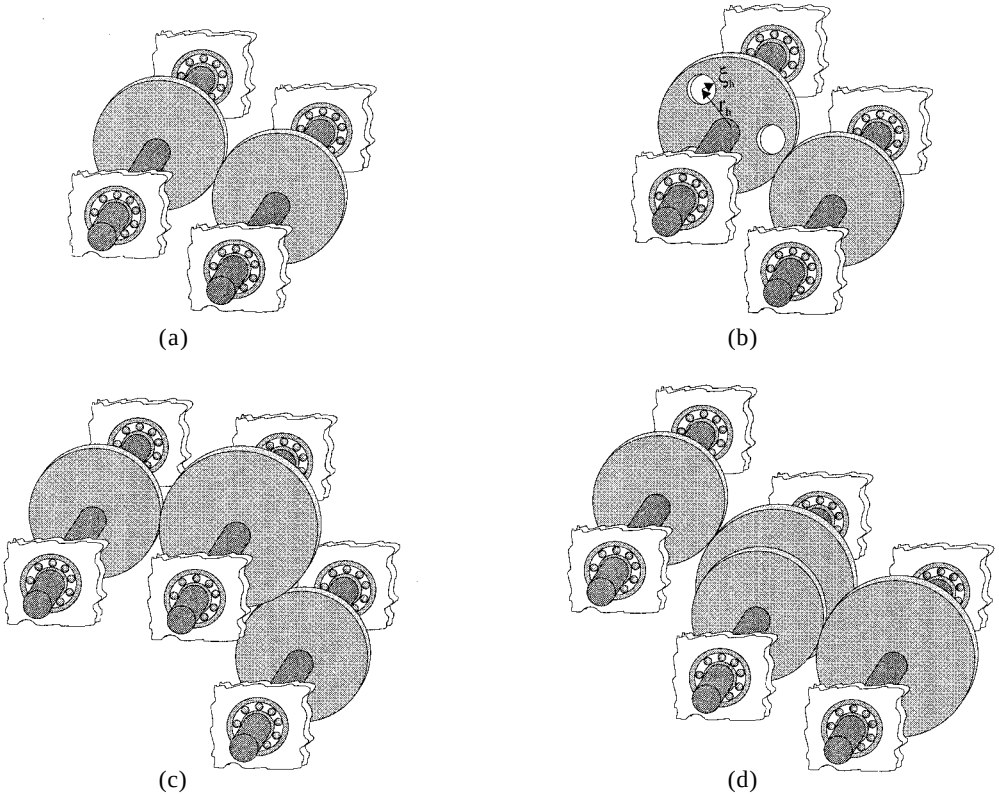

Figure 1. Example case: geared transmission systems. (a) Single mesh, (b) single mesh complex gear geometry, (c) dual mesh reverse idler, and (d) dual speed reducer.

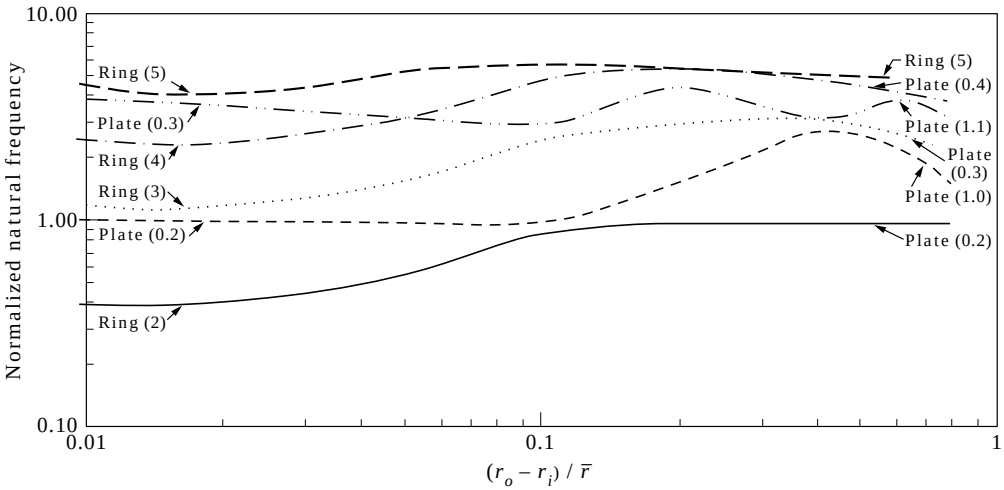

Figure 2. Normalized natural frequencies of a gear-like disk with respect to the out of plane (0, 2) mode of an annular plate. Here (m, n) represents a plate mode with m nodal circles and n nodal diameters while (n) represents an in-plane ring (radial direction) mode with n nodal diameters. ——, $r = 1$; – – –, $r = 2$; -----, $r = 3$; –·–·–, $r = 4$; –··–··–, $r = 5$; · · · ·, $r = 6$.

where $\mathbf{M}^i$ is the inertia matrix, $\mathbf{C}_m^{ij-i}$ and $\mathbf{C}_m^{ij-j}$ are the generalized damping matrices, $\mathbf{K}_m^{ij-i}$ and $\mathbf{K}_m^{ij-j}$ are the generalized mesh stiffness matrices, $\mathbf{K}_{sb}^i$ is the generalized shaft-bearing stiffness matrix, $\mathbf{K}_{ff}^i$ is the generalized structural stiffness matrix for the gear blank i, $\mathbf{Q}_{m\epsilon}^i$ is the internal force due to transmission error but it includes parametric effects associated

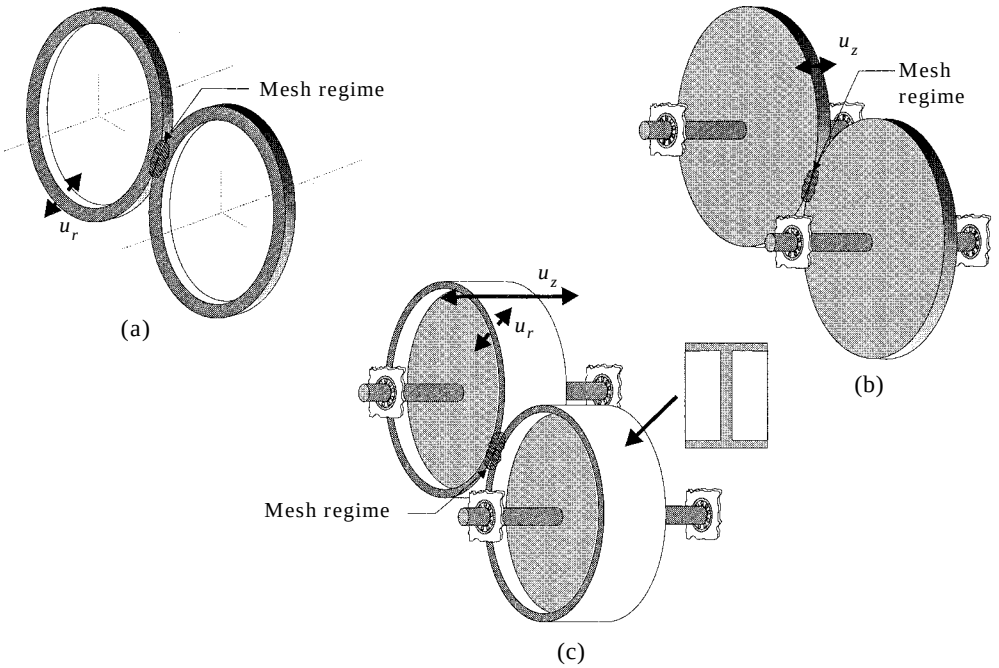

Figure 3. Modelling schemes used to describe compliant gear bodies; (a) Ring theory, (b) plate theory, and (c) numerically obtained eigensolutions or shape functions.

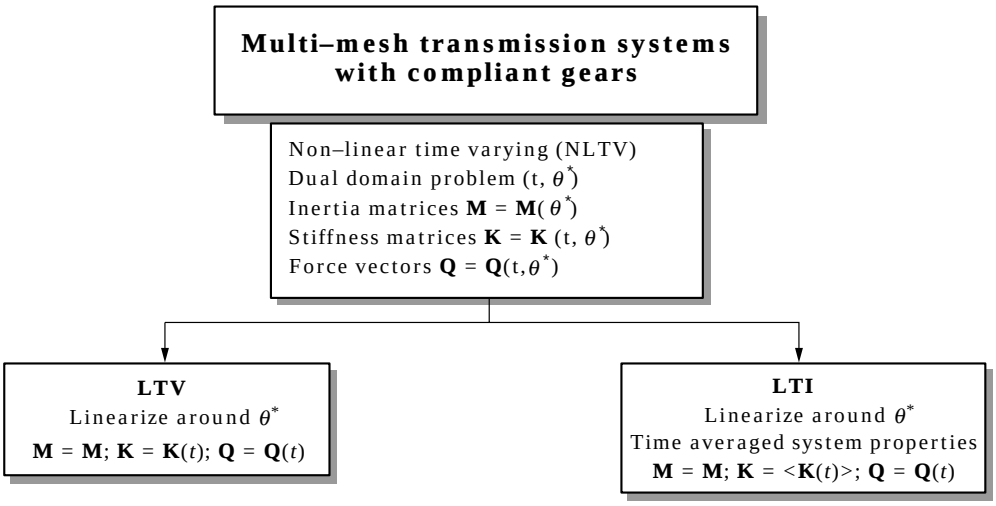

(a)

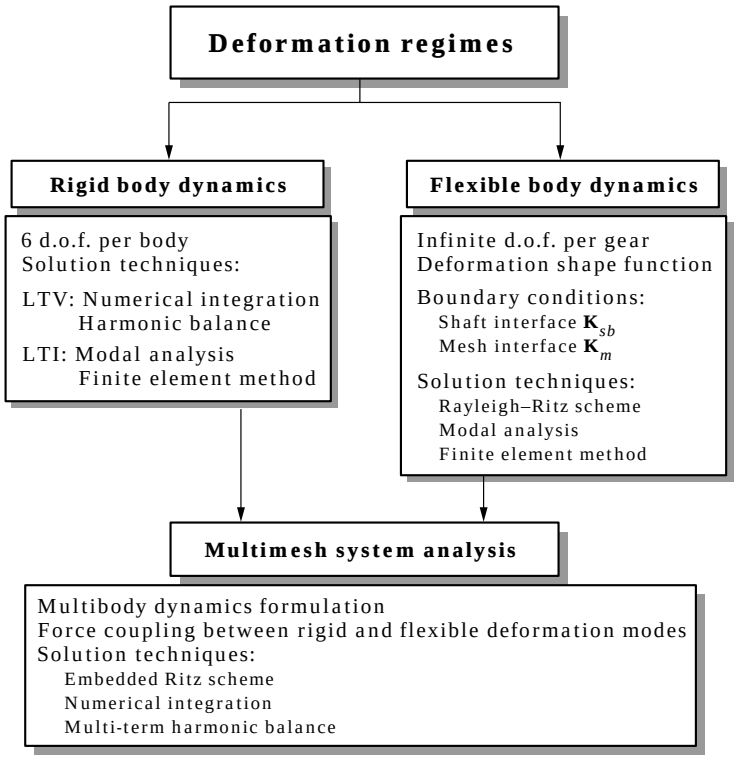

(b)

Figure 4. Formulation flowchart. (a) Simplification scheme from NLTV and LTI formulation, and (b) multi-body formulation scheme with compliant gear bodies.

with $\mathbf{K}_m^{ij-j}(\theta^{i*})$, $\mathbf{Q}^i$ is the external generalized force on gear i and $\mathbf{q}_m^i$ is the generalized co-ordinate associated with the gear i. The "pseudo forces" $\mathbf{Q}_{mg}^{ij-i*}(\Omega^*, t)$ and $\mathbf{Q}_{mg}^{ij-j^*}(\Omega^*, t)$ arise due to the coupling between the finite mean rotation of the gear with respect to the mesh ij and the flexible deformation of the gear blank itself (see the Appendix for identification of symbols).

The co-ordinate systems for a typical gear pair are given in detail in an earlier paper by the authors [9]. For the sake of clarity, a brief discussion together with the modifications necessary to represent the flexibility of the gear blanks is presented here. Figure 5 shows a few co-ordinate systems for a typical external gear body where X–Y–Z is an inertial reference frame and $\mathbf{X}_G^i - \mathbf{Y}_G^i - \mathbf{Z}_G^i$ and $\mathbf{X}_{Gm}^i - \mathbf{Y}_{Gm}^i - \mathbf{Z}_{Gm}^i$ are non-inertial frames necessary to completely define the motion of the gear body. Body co-ordinate system $\mathbf{X}_G^i - \mathbf{Y}_G^i - \mathbf{Z}_G^i$ is fixed to the gear blank i and hence it represents the true motion of the gear. The generalized co-ordinates of each gear are given as $\mathbf{q}^i = [\mathbf{R}_G^{iT}\ q^{iT}\mathbf{q}_f^{iT}]^T$, where $\mathbf{R}_G^i$ is the rigid body translational, θ^i is the rigid body rotational and $\mathbf{q}_f^i$ is the gear blank flexibility co-ordinates as defined in an earlier paper by Vinayak *et al*. [9]. The decomposition of these co-ordinates into a mean (subscript o) and a dynamic (subscript m) component is carried out as outlined by Blankenship and Singh [8] and it is assumed that the dynamic components are small compared to the corresponding mean components.

The origin of the geometric co-ordinate system $\mathbf{X}_{Gm}^i - \mathbf{Y}_{Gm}^i - \mathbf{Z}_{Gm}^i$ is coincident with that of the body co-ordinate and is fixed to the gear blank. This co-ordinate system however is a non-rotating type and its orientation is represented only by the dynamic component. The translational motion of this and the body co-ordinate system consists of the mean and vibratory components. The mean motion is significant for non-fixed centered gears i.e., planet gears in an epicyclic transmission system. A mesh co-ordinate system $\chi^{ij} - \gamma^{ij} - \phi^{ij}$ is fixed at the pitch point. Here $\gamma^{ij} - \phi^{ij}$ lie in the plane of action while χ^{ij} is normal to it, and ϕ^{ij} is parallel to the z-axis in the initial state. Yet another co-ordinate system $\chi^{ij} - \sigma^{ij} - \eta^{ij}$ is necessary for the helical gears when the line of action is inclined at an helix angle of Ψ_b^{ij} to ϕ^{ij}. For a spur gear, $\sigma^{ij} - \eta^{ij}$ and $\gamma^{ij} - \phi^{ij}$ are equivalent.

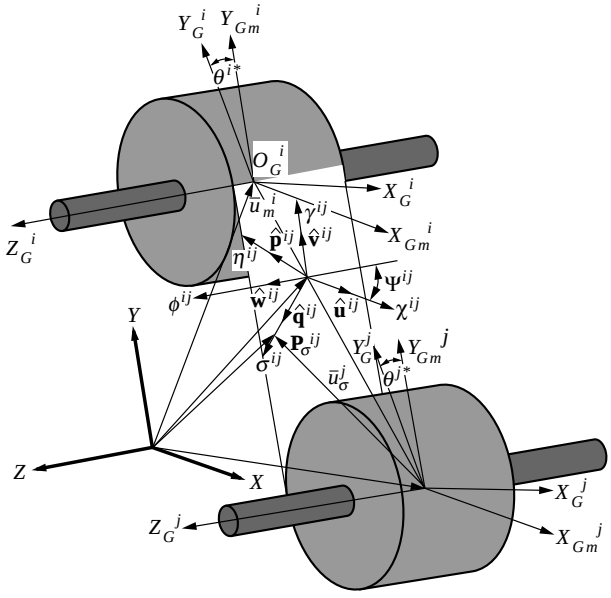

Figure 5. Schematic of the gear mesh with associated co-ordinate systems.

3.2. DYNAMIC MESH FORCE FORMULATION FOR COMPLIANT GEARS

A six dimensional mesh force vector concept was introduced by Blankenship and Singh [8, 38] and Vinayak and Singh [9] as $\mathbf{Q}^{ij}(t) = \mathbf{Q}^{ij}_o(t) + \mathbf{Q}^{ij}_m(t) = [\mathbf{F}^{ij}(t)^T \ \mathbf{T}^{ij}(t)^T]^T$ where $\mathbf{Q}^{ij}_o(t)$ and $\mathbf{Q}^{ij}_m(t)$ are mean and vibratory components respectively. The dynamic component $\mathbf{Q}^{ij}_m(t) = \mathbf{Q}^{ij}_{me}(t) + \mathbf{Q}^{ij}_{md}(t)$ consists of an elastic force $\mathbf{Q}^{ij}_{me}(t)$ and a dissipative force $\mathbf{Q}^{ij}_{md}(t)$. The elastic mesh force $\mathbf{Q}^{ij}_{me}(t) = \mathbf{Q}^{ij}_{mg}(t) + \mathbf{Q}^{ij}_{m\epsilon}(\theta^i*)$ consists of $\mathbf{Q}^{ij}_{mg}(t) = \mathbf{K}^{ij}_m(t)[\delta^i_q - \delta^j_q]$, where $\delta^i_q - \delta^j_q$ is the gross motion of the blanks and an internal, parametric excitation force $\mathbf{Q}^{ij}_{m\epsilon}(t) = \mathbf{K}^{ij}_m(t)[\delta^i_\epsilon - \delta^j_\epsilon]$ due to the static transmission error STE $= \delta^{ij}_\epsilon = \delta^i_\epsilon - \delta^j_\epsilon$. Here, $\mathbf{K}^{ij}_m$ is the generalized mesh stiffness matrix.

The analytical model of reference [9] is modified to include the effects of flexible gear blanks. Consider an external helical gear of Figure 5 as described in the mesh co-ordinates $\chi^{ij} - \sigma^{ij} - \eta^{ij}$. The mesh is modelled by a linear array of springs distributed over the length of contact Γ^{ij}, as proposed in references [8, 9], which depends on the tooth surface modifications, gear shaft misalignments and other mounting errors. The net contact zone may be off-center on the tooth facewidth say by a length h^{ij}. The elastic mesh force $\mathbf{F}^{ij}_{\sigma^{ij}}$ at a point P_{σ^i} in the direction $\hat{\mathbf{p}}^{ij}$, is

$$\| \mathbf{F}^{ij}_{\sigma^j}(t) \| = K^{ij}(t) \| [\delta \mathbf{r}^i_{P_{\sigma^{ij}}} - \delta \mathbf{r}^j_{P_{\sigma^{ij}}}] \| \, \delta\sigma, \tag{2}$$

where $K^{ij}(t)$ is a scalar value for mesh stiffness per unit length of contact. Here $\mathbf{r}^i_{P_{\sigma^{ij}}}$ and $\mathbf{r}^j_{P_{\sigma^{ij}}}$ give the position of $P_{\sigma^{ij}}$ in the geometric co-ordinates attached to the gears i and j, respectively, as

$$\mathbf{r}^i_{P_{\sigma^j}} = \mathbf{R}^i_G + \mathbf{A}^i \bar{\mathbf{u}}^i_{\sigma^{ij}}, \qquad \mathbf{r}^j_{P_{\sigma^j}} = \mathbf{R}^j_G + \mathbf{A}^j \bar{\mathbf{u}}^j_{\sigma^{ij}}. \tag{3a, b}$$

The position vectors $\bar{\mathbf{u}}^i_{\sigma^{ij}}$ and $\bar{\mathbf{u}}^j_{\sigma^{ij}}$ are in the geometric co-ordinates ($\mathbf{X}^i_{Gm}$–$\mathbf{Y}^i_{Gm}$–$\mathbf{Z}^i_{Gm}$) and ($\mathbf{X}^j_{Gm}$–$\mathbf{Y}^j_{Gm}$–$\mathbf{Z}^j_{Gm}$) of gears i and j respectively and are given as follows where $\bar{\mathbf{u}}^i_{\sigma^{ijr}}$ and $\bar{\mathbf{u}}^j_{\sigma^{ijr}}$ are the new position co-ordinates of P_{σ^i} with respect to gears i and j due to rigid body rotation and $\bar{\mathbf{u}}^i_{\sigma^{ijf}}$ and $\bar{\mathbf{u}}^j_{\sigma^{ijf}}$ are the additonal changes in position co-ordinate of P_{σ^j} due to the flexible distortion of the gear bodies i and j respectively:

$$\bar{\mathbf{u}}^i_{\sigma^j} = \bar{\mathbf{u}}^i_{\sigma^{ijr}} + \bar{\mathbf{u}}^i_{\sigma^{ijf}}, \qquad \bar{\mathbf{u}}^j_{\sigma^j} = \bar{\mathbf{u}}^j_{\sigma^{ijr}} + \bar{\mathbf{u}}^j_{\sigma^{ijf}}. \tag{4a, b}$$

The displacements due to the flexibility of gear blanks $\bar{\mathbf{u}}^i_{\sigma^{ijf}}$ and $\bar{\mathbf{u}}^j_{\sigma^{ijf}}$ have been extensively characterized by Vinayak and Singh in a separate article [23]. They are given as follows where $\mathbf{q}^i_f(t)$ and $\mathbf{q}^j_f(t)$ are the flexibility co-ordinates and $\mathbf{S}^i_{\sigma^{ij}}(x^i_{G_{\sigma^{ij}}}, y^i_{G_{\sigma^{ij}}}, z^i_{G_{\sigma^{ij}}})$ and $\mathbf{S}^j_{\sigma^{ij}}(x^j_{G_{\sigma^{ij}}}, y^j_{G_{\sigma^{ij}}}, z^j_{G_{\sigma^{ij}}})$ are the shape function matrices comprised of complete orthogonal sets of functions describing the deformable body:

$$\bar{\mathbf{u}}^i_{\sigma^{ijf}} = \mathbf{S}^i_{\sigma^{ij}}(x^i_{G_{\sigma^{ij}}}, y^i_{G_{\sigma^{ij}}}, z^i_{G_{\sigma^{ij}}}) \mathbf{q}^i_f(t), \qquad \bar{\mathbf{u}}^j_{\sigma^{ijf}} = \mathbf{S}^j_{\sigma^{ij}}(x^j_{G_{\sigma^{ij}}}, y^j_{G_{\sigma^{ij}}}, z^j_{G_{\sigma^{ij}}}) \mathbf{q}^j_f(t). \tag{5a, b}$$

Here, $x^i_{G_{\sigma^{ij}}}, y^i_{G_{\sigma^{ij}}}, z^i_{G_{\sigma^{ij}}}$ and $x^j_{G_{\sigma^{ij}}}, y^j_{G_{\sigma^{ij}}}, z^j_{G_{\sigma^{ij}}}$ are the position co-ordinates of $P_{\sigma^{ij}}$ in the gear co-ordinate systems of gears i and j respectively. Further, $\mathbf{A}^i$ and $\mathbf{A}^j$ are the rotational transformation matrices formed for these co-ordinate systems given as

$$\mathbf{A}^i(t) = \begin{bmatrix} 1 & -\theta^i_{zm} & \theta^i_{ym} \\ \theta^i_{zm} & 1 & -\theta^i_{xm} \\ -\theta^i_{ym} & \theta^i_{xm} & 1 \end{bmatrix}, \qquad \mathbf{A}^j(t) = \begin{bmatrix} 1 & -\theta^j_{zm} & \theta^j_{ym} \\ \theta^j_{zm} & 1 & -\theta^j_{xm} \\ -\theta^j_{ym} & \theta^j_{xm} & 1 \end{bmatrix}, \tag{5c, d}$$

where angles $\theta^{i,j}_{xm}$, $\theta^{i,j}_{ym}$, $\theta^{i,j}_{zm}$ are assumed to be very small such that $\cos\theta^{i,j}_{xm} \approx 1$ and $\sin\theta^{i,j}_{xm} \approx \theta^{i,j}_{xm}$, etc.

Now, $\delta \mathbf{r}^i_{P_\sigma{}^{ij}}$ and $\delta \mathbf{r}^j_{P_\sigma{}^{ij}}$ can be derived from equation (3) as $\delta \mathbf{r}^i_{P_\sigma{}^{ij}} = \delta \mathbf{R}^i_G + \delta(\mathbf{A}^i \bar{\mathbf{u}}^i_{\sigma^{ij}})$ and $\delta \mathbf{r}^j_{P_\sigma{}^{ij}} = \delta \mathbf{R}^j_G + \delta(\mathbf{A}^j \bar{\mathbf{u}}^j_{\sigma^{ij}})$. Since $\langle \theta^{i,j}_{xm} \rangle = 0$ and $\langle \mathbf{R}^i_G \rangle = 0$, where $\langle\ \rangle$ denotes a spatial position mean, $\delta\theta^{i,j}_{xm} = \theta^{i,j}_{xm}$ and $\delta \mathbf{R}^i_G = \mathbf{R}^i_{Gm}$, etc., we get

$$\delta \mathbf{r}^i_{P_\sigma{}^{ij}}(t) = \mathbf{R}^i_{Gm} + \mathbf{A}^i \tilde{\bar{\mathbf{u}}}^{iT}_{\sigma^{ij}} \mathbf{G}^i q^i_m + \mathbf{A}^i \delta \bar{\mathbf{u}}^i_{\sigma^{ij}}, \qquad \delta \mathbf{r}^j_{P_\sigma{}^{ij}}(t) = \mathbf{R}^j_{Gm} + \mathbf{A}^j \tilde{\bar{\mathbf{u}}}^{jT}_{\sigma^{ij}} \mathbf{G}^j q^j_m + \mathbf{A}^j \delta \bar{\mathbf{u}}^j_{\sigma^{ij}}. \quad \text{(6a, b)}$$

Here, $\omega^{i,j} = \mathbf{G}^{i,j} q^{i,j}_m$ is the angular velocity and $q^{i,j}_m = [\theta^{i,j}_{xm}\ \ \theta^{i,j}_{ym}\ \ \theta^{i,j}_{zm}]^T$ where the superscript T implies the transpose. Since $\theta^{i,j}_m$'s are infinitesimally small, $\omega^i \approx q^i_m$ and $\mathbf{G}^i \approx \mathbf{I}$, where $\mathbf{I}$ is an identity matrix. Further, $\tilde{\bar{\mathbf{u}}}^{i,j}_\sigma$ is an asymmetrical matrix formed from $\bar{\mathbf{u}}^{i,j}_\theta = [\bar{u}^{i,j}_{\sigma\theta_x}\ \ \bar{u}^{i,j}_{\sigma\theta_y}\ \ \bar{u}^{i,j}_{\sigma\theta_z}]^T$ and is given by

$$\tilde{\bar{\mathbf{u}}}^{i,j}_\theta(t) = \begin{bmatrix} 0 & -\bar{u}^{i,j}_{\sigma\theta_z} & \bar{u}^{i,j}_{\sigma\theta_y} \\ \bar{u}^{i,j}_{\sigma\theta_z} & 0 & -\bar{u}^{i,j}_{\sigma\theta_x} \\ -\bar{u}^{i,j}_{\sigma\theta_y} & \bar{u}^{i,j}_{\sigma\theta_x} & 0 \end{bmatrix}$$

$$= \begin{bmatrix} 0 & -\bar{u}^{i,j}_{\sigma\theta_{zr}} & \bar{u}^{i,j}_{\sigma\theta_{yr}} \\ \bar{u}^{i,j}_{\sigma\theta_{zr}} & 0 & -\bar{u}^{i,j}_{\sigma\theta_{xr}} \\ -\bar{u}^{i,j}_{\sigma\theta_{yr}} & \bar{u}^{i,j}_{\sigma\theta_{xr}} & 0 \end{bmatrix} + \begin{bmatrix} 0 & -\bar{u}^{i,j}_{\sigma\theta_{zf}} & \bar{u}^{i,j}_{\sigma\theta_{yf}} \\ \bar{u}^{i,j}_{\sigma\theta_{zf}} & 0 & -\bar{u}^{i,j}_{\sigma\theta_{xf}} \\ -\bar{u}^{i,j}_{\sigma\theta_{yf}} & \bar{u}^{i,j}_{\sigma\theta_{xf}} & 0 \end{bmatrix}. \quad (7)$$

With reference to Figure 5, $\bar{\mathbf{u}}^{i,j}_{\sigma\theta_r}$ can be given by the sum of $\bar{\mathbf{u}}^{i,j}_{mr}$, position vector of the pitch point in geometric co-ordinates and the unit mesh vector $\hat{\mathbf{q}}^{ij}$ as $\bar{\mathbf{u}}^{i,j}_{\sigma\theta_r} = \bar{\mathbf{u}}^{i,j}_{mr} + \sigma^{ij}\hat{\mathbf{q}}^{ij}$. The pitch position vectors are $\bar{\mathbf{u}}^i_m = \mathbf{A}^{iT}\xi[\mathbf{R}^j_G - \mathbf{R}^i_G]$ and $\bar{\mathbf{u}}^j_m = \mathbf{A}^{jT}\xi[\mathbf{R}^j_G - \mathbf{R}^i_G]$, where $\xi = \phi^i/(\phi^i + \phi^j)$. These can now be used to obtain an expression for $\delta\bar{\mathbf{u}}^i_{\sigma^{ij}}\ \delta\bar{\mathbf{u}}^j_{\sigma^{ij}}$ as

$$\delta\bar{\mathbf{u}}^i_{\sigma^{ij}}(t) = \xi\delta[\mathbf{A}^{iT}(t)\,(\mathbf{R}^j_G(t, \theta^{i*}) - \mathbf{R}^i_G(t, \theta^{i*}))] + \sigma^{ij}\delta\hat{q}^{ij} + \delta\bar{\mathbf{u}}^i_{\sigma^{ij}f}(t), \quad \text{(8a)}$$

$$\delta\bar{\mathbf{u}}^j_{\sigma^{ij}}(t) = \xi\delta[\mathbf{A}^{jT}(t)\,(\mathbf{R}^j_G(t, \theta^{i*}) - \mathbf{R}^j_G(t, \theta^{i*}))] + \sigma^{ij}\delta\hat{q}^{ij} + \delta\bar{\mathbf{u}}^j_{\sigma^{ij}f}(t). \quad \text{(8b)}$$

Expressions for the mesh unit vectors $\hat{\mathbf{u}}^{ij}$, $\hat{\mathbf{v}}^{ij}$, $\hat{\mathbf{q}}^{ij}$ and $\hat{\mathbf{p}}^{ij}$ have already been derived by Blankenship and Singh [8]. These can be used to obtain

$$\delta\hat{\mathbf{q}}^{ij} = \delta\left[\mathbf{L}^i_u \begin{Bmatrix} \hat{\mathbf{u}}^{ij} \\ \hat{\mathbf{v}}^{ij} \end{Bmatrix}\right]$$

where

$$\begin{bmatrix} \mathbf{L}^i_u \\ \mathbf{L}^i_v \end{bmatrix} = \begin{bmatrix} \cos\Psi^i_b & -\sin\Psi^i_b \\ \sin\Psi^i_b & \cos\Psi^i_b \end{bmatrix}.$$

These, together with expressions for

$$\delta\bar{\mathbf{u}}^i_{\sigma^{ij}f}(t) = \delta[\mathbf{S}^i_{\sigma^{ij}}(x^i_{G_\sigma{}^{ij}}, y^i_{G_\sigma{}^{ij}}, z^i_{G_\sigma{}^{ij}})\mathbf{q}^i_f(t)] \quad \text{and} \quad \delta\bar{\mathbf{u}}^j_{\sigma^{ij}f}(t) = \delta[\mathbf{S}^j_{\sigma^{ij}}(x^j_{G_\sigma{}^{ij}}, y^j_{G_\sigma{}^{ij}}, z^j_{G_\sigma{}^{ij}})\mathbf{q}^j_f(t)],$$

obtained from equation (5a) are substituted into equation (8) to give

$$\delta\mathbf{r}^i_{P_\sigma{}^{ij}}(t, \theta^{i*}) = \mathbf{R}^i_{Gm}(t) - \mathbf{A}^i(t)\tilde{\bar{\mathbf{u}}}^i_{\sigma^{ij}}(t, \theta^{i*})q^i_m(t) + \xi\mathbf{A}^i(t)\delta[\mathbf{A}^{iT}(t)\{\mathbf{R}^j_G(t, \theta^{i*}) - \mathbf{R}^i_G(t, \theta^{i*})\}]$$

$$+ \sigma^{ij}\mathbf{A}^i(t)\delta\left[\mathbf{L}^i_u \begin{Bmatrix} \mathbf{A}^i(t)\hat{\mathbf{u}}^{ij} \\ \mathbf{A}^i(t)\hat{\mathbf{v}}^{ij} \end{Bmatrix}\{\mathbf{R}^j_G(t, \theta^{i*}) - \mathbf{R}^i_G(t, \theta^{i*})\}\right]$$

$$+ \mathbf{A}^i(t)\delta[\mathbf{S}^i_{\sigma^{ij}}(x^i_{G_\sigma{}^{ij}}, y^i_{G_\sigma{}^{ij}}, z^i_{G_\sigma{}^{ij}})\mathbf{q}^i_f(t)], \quad \text{(9a)}$$

$$\delta \mathbf{r}^j_{P_{\sigma^{ij}}}(t, \theta^{j*}) = \mathbf{R}^j_{Gm}(t) - \mathbf{A}^j(t)\tilde{\mathbf{u}}^j_{\sigma^{ij}}(t, \theta^{j*})q^j_m(t) + \xi \mathbf{A}^j(t)\delta[\mathbf{A}^{jT}(t)\{\mathbf{R}^i_G(t, \theta^{i*}) - \mathbf{R}^j_G(t, \theta^{i*})\}]$$

$$+ \sigma^{ij}\mathbf{A}^j(t)\delta\left[\mathbf{L}^j_u \begin{Bmatrix} \mathbf{A}^j(t)\hat{\mathbf{u}}^{ji} \\ \mathbf{A}^j(t)\hat{\mathbf{v}}^{ji} \end{Bmatrix}\{\mathbf{R}^i_G(t, \theta^{j*}) - \mathbf{R}^j_G(t, \theta^{j*})\}\right]$$

$$+ \mathbf{A}^j(t)\delta[\mathbf{S}^j_{\sigma^{ij}}(x^j_{G_{\sigma^{ij}}}, y^j_{G_{\sigma^{ij}}}, z^j_{G_{\sigma^{ij}}})\mathbf{q}^j_f(t)]. \tag{9b}$$

These can be used to determine $\delta \mathbf{r}^j_{P_{\sigma^{ij}}}$ and $\delta \mathbf{r}^j_{P_{\sigma^{ij}}}$ at any instant of time t and nominal angular positions θ^{i*} and θ^{j*}. Subsequently, the instantaneous mesh force $\mathbf{F}^{ij}_{\sigma^{ij}}$ at the point $P_{\sigma^{ij}}$ can be obtained. The generalized force $\mathbf{Q}^{ij}_{mg\sigma^{ij}}$ due to the instantaneous mesh point force $\mathbf{F}^{ij}_{\sigma^{ij}}$ is given by

$$\mathbf{Q}^{ij}_{mg\sigma^{ij}} \approx [\mathbf{I} \;\; \mathbf{A}^i\tilde{\mathbf{u}}^{iT}_{\sigma^{ij}} \;\; \mathbf{A}^i\mathbf{S}^i]^T\mathbf{F}^{ij}_{\sigma^{ij}} = [\mathbf{I} \;\; \mathbf{A}^i\tilde{\mathbf{u}}^{iT}_{\sigma^j} \;\; \mathbf{A}^i\mathbf{S}^i]^T\hat{\mathbf{p}}^{ij} \| \mathbf{F}^{ij}_{\sigma^{ij}} \|.$$

Substitution in equation (2) yields

$$\mathbf{Q}^{ij}_{mg\sigma^{ij}}(t, \theta^{i*}) \approx \begin{bmatrix} \mathbf{I} \\ \tilde{\mathbf{u}}^i_{\sigma^{ij}}\mathbf{A}^{iT} \\ \mathbf{S}^{iT}\mathbf{A}^{iT} \end{bmatrix}\hat{\mathbf{p}}^{ij}K^{ij}\hat{\mathbf{p}}^{ijT}\{\delta \mathbf{r}^i_{P_{\sigma^{ij}}}(t, \theta^{i*}) - \delta \mathbf{r}^i_{P_{\sigma^{ij}}}(t, \theta^{j*})\}\delta\sigma. \tag{10}$$

Assuming that the contact occurs over the entire zone of contact along the line of action between gears i and j, the total generalized mesh force on gear i is

$$\mathbf{Q}^{ij}_{mg}(t, \theta^{i*}) = \int_{h^{ij} - \Gamma^{ij}/2}^{h^{ij} + \Gamma^{ij}/2} \left(\begin{bmatrix} \mathbf{I} \\ \tilde{\mathbf{u}}^i_{\sigma^{ij}}\mathbf{A}^{iT} \\ \mathbf{S}^{iT}\mathbf{A}^{iT} \end{bmatrix}\hat{\mathbf{p}}^{ij}K^{ij}\hat{\mathbf{p}}^{ijT}\{\delta \mathbf{r}^i_{P_{\sigma^{ij}}}(t, \theta^{i*}) - \delta \mathbf{r}^i_{P_{\sigma^{ij}}}(t, \theta^{j*})\} \right) \mathrm{d}\sigma. \tag{11}$$

Similarly, the parametric excitation force $\mathbf{Q}^{ij}_{m\epsilon}$ due to kinematic errors between teeth and elastic deflections of teeth is

$$\mathbf{Q}^{ij}_{m\epsilon}(t, \theta^{i*}) = \int_{h^{ij} - \Gamma^{ij}/2}^{h^{ij} + \Gamma^{ij}/2} \left(\begin{bmatrix} \mathbf{I} \\ \tilde{\mathbf{u}}^i_{\sigma^{ij}}\mathbf{A}^{iT} \\ \mathbf{S}^{iT}\mathbf{A}^{iT} \end{bmatrix}\hat{\mathbf{p}}^{ij}K^{ij}\hat{\mathbf{p}}^{ijT} \right) \mathrm{d}\sigma(\delta^i_{\epsilon m} - \delta^j_{\epsilon m}), \tag{12}$$

where δ^i_ϵ and δ^j_ϵ are three dimensional transmission error vectors described in the mesh co-ordinates $(\chi^{ij} - \sigma^{ij} - \eta^{ij})$.

3.3. LINEAR FORMULATION FOR Q AND K

The assumption of quasi-static state, i.e., limit $\Omega^* \to 0$, which was used to simplify the mesh force expression for systems containing rigid gears [16], is no longer valid when the gears are relatively compliant. Nevertheless the total generalized force on any gear can still be given in the t domain only as follows by assuming $\theta^* = \Omega^* t$ for a system rotating with a constant Ω^*:

$$\mathbf{Q}^{ij}_m(t) = \mathbf{Q}^{ij}_{mg}(t) + \mathbf{Q}^{ij}_{m\epsilon}(\delta^i_{\epsilon m}, \delta^j_{\epsilon m}, t) + \mathbf{Q}^{ij}_{md}(t). \tag{13}$$

Since the vibratory generalized co-ordinates θ^i_m, $\delta \mathbf{R}^i_G$ and $\mathbf{q}^i_{fm}$ are assumed to be small compared to mean components θ^i_o, $\mathbf{R}^i_{G_o}$ and $\mathbf{q}^i_{fo}$, any products of vibratory components can obviously be neglected. It is desirable at this juncture since equation (16) is non-linear with time and position varying coefficients. Solutions of such equations are very computationally intensive, especially for systems with multi-meshes. For instance, the third term of equation (9), $\mathbf{A}^i\delta(\tilde{\mathbf{u}}^i_{\sigma^{ij}})$ consists of some non-linear product of very small components which can be effectively neglected thereby reducing this term to

$\mathbf{A}^i(t)\delta[\mathbf{S}^i_{\sigma^{ij}}(x^i_{G_{\sigma^{ij}}}, y^i_{G_{\sigma^{ij}}}, z^i_{G_{\sigma^{ij}}})\mathbf{q}^i_f(t)]$. Here $\mathbf{S}^i_{\sigma^{ij}}(x^i_{G_{\sigma^{ij}}}, y^i_{G_{\sigma^{ij}}}, z^i_{G_{\sigma^{ij}}})$ is the shape function $P_{\sigma^j}(x^i_{G_{\sigma^{ij}}}, y^i_{G_{\sigma^{ij}}}, z^i_{G_{\sigma^{ij}}})$, a point on the line of action, which can be visualized as rotating in the gear body co-ordinate system with a velocity Ω^*. Thus $\delta\mathbf{S}^i_{\sigma^{ij}}(x^i_{G_{\sigma^{ij}}}, y^i_{G_{\sigma^{ij}}}, z^i_{G_{\sigma^{ij}}})$ can be quite large, resulting in no further simplification of this term. Similar simplifications are possible for the equations of gear j. Equations (9a and b) can now be reformulated as $\delta\mathbf{r}^i_{P_{\sigma^{ij}}} \approx \mathbf{R}^i_{Gm} + \mathbf{A}^i\tilde{\tilde{\mathbf{u}}}^T_{\sigma^{ij}}\, q^i_m + \mathbf{A}^i\mathbf{S}^i_{\sigma^{ij}}\,\mathbf{q}^i_{f_m} + \mathbf{A}^i\delta\mathbf{S}^i_{\sigma^{ij}}\,\mathbf{q}^i_f$ and $\delta\mathbf{r}^j_{P_{\sigma^{ij}}} \approx \mathbf{R}^j_{Gm} + \mathbf{A}^j\tilde{\tilde{\mathbf{u}}}^T_{\sigma^{ij}}\, q^j_m + \mathbf{A}^i\mathbf{S}^j_{\sigma^{ij}}\,\mathbf{q}^j_{f_m} + \mathbf{A}^j\delta\mathbf{S}^j_{\sigma^{ij}}\,\mathbf{q}^j_f$, which can be written in a compact form as follows, where $\mathbf{q}^i_m = [\mathbf{R}^{iT}_{Gm} \quad q^{iT}_m \quad \mathbf{q}^{iT}_{f_m}]^T$ and $\mathbf{q}^j_m = [\mathbf{R}^{jT}_{Gm} \quad q^{jT}_m \quad \mathbf{q}^{jT}_{f_m}]^T$ are the quasi-static generalized co-ordinates of gears i and j respectively:

$$\delta\mathbf{r}^i_{P_{\sigma^{ij}}}(t) \approx [\mathbf{I} \;\; \mathbf{A}^i\tilde{\tilde{\mathbf{u}}}^{iT}_{\sigma^{ij}} \;\; \mathbf{A}^i\mathbf{S}^i_{\sigma^{ij}}]\mathbf{q}^i_m + \mathbf{A}^i\delta\mathbf{S}^i_{\sigma^{ij}}\,\mathbf{q}^i_f, \qquad \delta\mathbf{r}^j_{P_{\sigma^{ij}}}(t) \approx [\mathbf{I} \;\; \mathbf{A}^j\tilde{\tilde{\mathbf{u}}}^{jT}_{\sigma^{ij}} \;\; \mathbf{A}^j\mathbf{S}^j_{\sigma^{ij}}]\mathbf{q}^j_m + \mathbf{A}^j\delta\mathbf{S}^j_{\sigma^{ij}}\,\mathbf{q}^j_f, \tag{14a, b}$$

The term $\hat{\mathbf{p}}^{ij}(t)K^{ij}\hat{\mathbf{p}}^{ijT}(t)$ of equations (11) and (12) is non-linear, and in dual domain i.e., it is time (t) and position (θ^i*) dependent. The unit mesh vector $\hat{\mathbf{p}}^{ij}$ can be decomposed into a mean $\hat{\mathbf{p}}^{ij}_o$ and a time varying component $\hat{\mathbf{p}}^{ij}_m$ as $\hat{\mathbf{p}}^{ij}(t) = \hat{\mathbf{p}}^{ij}_o(\mathbf{R}^i_o, \mathbf{R}^j_o, \theta^i{*}) + \hat{\mathbf{p}}^{ij}_m(t)$. Since the time varying component is very small, it can also be neglected. Thus the above mentioned term reduces to $\hat{\mathbf{p}}^{ij}_o(\theta^i{*})K^{ij}\hat{\mathbf{p}}^{ijT}_o(\theta^i{*})$ where t is effectively replaced by θ^i*. Substituting this and equation (14) in equation (2) and replacing $\mathbf{A}^i$ by an identity matrix $\mathbf{I}$ since θ^i_m's are small, we get

$$\mathbf{Q}^{ij}_{mg}(t) = \mathbf{Q}^{ij-i}_{mg}(t) - \mathbf{Q}^{ij-j}_{mg}(t). \tag{15}$$

Here, $\mathbf{Q}^{ij-i}_{mg}(t) = \mathbf{K}^{ij-i}_m\,\mathbf{q}^i_m + \mathbf{Q}^{ij-i*}_{mg}(\Omega^*, t)$ is the mesh force on gear i due to the motion of gear body i and $\mathbf{Q}^{ij-i}_{mg}(t) = \mathbf{K}^{ij-j}_m\,\mathbf{q}^j_m + \mathbf{Q}^{ij-j*}_{mg}(\Omega^*, t)$ is the mesh force on gear i due to the motion of gear body j. The non-linear, dual domain terms $\mathbf{Q}^{ij-i*}_{mg}(\Omega^*, t)$ and $\mathbf{Q}^{ij-j*}_{mg}(\Omega^*, t)$ appear due to the coupling of the gear blank deformation shape functions and the finite mean rotation of the gears θ^* and they are given by the following expression:

$$\mathbf{Q}^{ij-\ell*}_{mg}(\Omega^*, t) = \int_{h^{ij}(\theta^{i*})-\Gamma^{ij}(\theta^{i*})/2}^{h^{ij}(\theta^{i*})+\Gamma^{ij}(\theta^{i*})/2} \begin{bmatrix} \mathbf{I} \\ \tilde{\tilde{\mathbf{u}}}^i_{\sigma^{ij}}(\theta^{i*}) \\ \mathbf{S}^{iT}_{\sigma^{ij}} \end{bmatrix} \hat{\mathbf{p}}^{ij}_o(\theta^{i*})K^{ij}\hat{\mathbf{p}}^{ijT}_o(\theta^{i*})\delta\mathbf{S}^\ell_{\sigma^{ij}}\,\mathbf{q}^\ell_f(t)\,\mathrm{d}\sigma, \quad \ell = i, j. \tag{16}$$

Similarly the mesh stiffness $\mathbf{K}^{ij-i}_m$ and $\mathbf{K}^{ij-j}_m$ are given as

$$\mathbf{K}^{ij-\ell}_m(\theta^{i*}) = \int_{h^i(\theta^{i*})-\Gamma^i(\theta^{i*})/2}^{h^i(\theta^{i*})+\Gamma^i(\theta^{i*})/2} \begin{bmatrix} \mathbf{I} \\ \tilde{\tilde{\mathbf{u}}}^i_{\sigma^i}(\theta^{i*}) \\ \mathbf{S}^{iT}_{\sigma^{ij}} \end{bmatrix} \hat{\mathbf{p}}^{ij}_o(\theta^{i*})K^{ij}\hat{\mathbf{p}}^{ijT}_o(\theta^{i*})\,[\mathbf{I} \;\; \tilde{\tilde{\mathbf{u}}}^{\ell T}_{\sigma^{ij}}(\theta^{i*}) \;\; \mathbf{S}^\ell_{\sigma^{ij}}]\,\mathrm{d}\sigma, \quad \ell = i, j. \tag{17}$$

This expression for mesh stiffness is similar to the formulation of reference [9] but it has additional terms which are obviously related to the elastic deformation modes of gear blanks. It is still linear with normal position varying coefficients. Again, the offset $h^{ij}(\theta^{i*})$ and contact length $\Gamma^{ij}(\theta^{i*})$ can be obtained from the existing gear contact mechanics programs [31]. Also the stiffness per unit length K^{ij} can be estimated from such programs. This scheme is shown in a flowchart form in Figure 4(a).

Finally, for the sake of comparison with existing finite element solutions, this model can be reduced to an LTI form. This can be ahcieved by assuming that the force coupling term due to the finite rotation of the gears $\mathbf{Q}^{ij-i*}_{mg}(\Omega^*, t)$ and $\mathbf{Q}^{ij-j*}_{mg}(\Omega^*, t)$ are negligible although this is not always valid since the rotation speed Ω^* is often high. Further $h^{ij}(\theta^{i*})$ and $\Gamma^{ij}(\theta^{i*})$ can be decomposed into mean and θ^{i*} varying components as $h^{ij}(\theta^{i*}) = h^{ij}_o + h^{ij}_m(\theta^{i*})$ and $\Gamma^{ij}(\theta^{i*}) = \Gamma^{ij}_o + \Gamma^{ij}_m(\theta^{i*})$. Now, the θ^{i*} varying components can be neglected to give a linear expression for mesh stiffness with position-invariant coefficients.

Again, this model may not be accurate since the oscillatory components are not usually negligible. Nonetheless, this model yields an eigenvalue problem which can be very easily solved to gain an insight into the dynamic characteristics of the geared system.

4. REDUCED GEAR MESH EXPRESSIONS

4.1. REDUCED MESH EXPRESSIONS USING FLEXURAL PLATE THEORY

For a relatively thin compliant gear (thickness/radius $< 0{\cdot}1$) as shown in Figure 3(a), the plate flexural theory may be used to describe the transverse (normal to the gear body) motions. Also, for most thin gears, (excluding ring and thin rimmed gears which will be studied in section 3.2), the radial motion (towards the mesh) can be neglected since the radial stiffness is relatively high compared to the transverse stiffness. With these assumptions, equations (14a and b) can be reduced as follows, where $\tilde{\bar{\mathbf{u}}}^i_{\sigma^{ij}} = [-\bar{\mathbf{u}}^i_{\sigma^{ij}{}_v}\ \ \bar{\mathbf{u}}^i_{\sigma^{ij}{}_x}\ \ 0]$ and $\tilde{\bar{\mathbf{u}}}^j_{\sigma^{ij}} = [-\bar{\mathbf{u}}^j_{\sigma^{ij}{}_v}\ \ \bar{\mathbf{u}}^j_{\sigma^{ij}{}_x}\ \ 0]$ are formed from mesh position vector and $\mathbf{q}^i_m = [\mathbf{R}^i_{Gm_x}\ \ \mathbf{R}^i_{Gm_y}\ \ q^i_{m_z}\ \ \mathbf{q}^i_{f_m}]$ and $\mathbf{q}^j_m = [\mathbf{R}^j_{Gm_x}\ \ \mathbf{R}^j_{Gm_y}\ \ q^j_{m_z}\ \ \mathbf{q}^j_{f_m}]$ are the generalized co-ordinates:

$$\mathbf{I}^* = \begin{bmatrix} 1 & 0 \\ 0 & 1 \\ 0 & 0 \end{bmatrix}, \qquad \delta\mathbf{r}^i_{P_{\sigma^{ij}}}(t) = [\mathbf{I}^*\ \ \tilde{\bar{\mathbf{u}}}^{iT}_{\sigma^{ij}}\ \ \mathbf{S}^i_{\sigma^{ij}}]\mathbf{q}^i_m, \qquad \delta\mathbf{r}^j_{P_{\sigma^{ij}}}(t) = [\mathbf{I}^*\ \ \tilde{\bar{\mathbf{u}}}^{jT}_{\sigma^{ij}}\ \ \mathbf{S}^j_{\sigma^{ij}}]\mathbf{q}^j_m. \quad (18a\text{–}c)$$

Here, matrices $\mathbf{S}^i_{\sigma^{ij}}$ and $\mathbf{S}^j_{\sigma^{ij}}$ are the shape functions $\mathbf{S}(r, \theta, z)$ evaluated at σ^{ij} for gears i and j respectively. Many gear blanks deviate considerably from annular plates because of rims, hubs, holes within the blanks as well as stiffeners that may be placed. Consequently, a new bi-orthogonal shape function matrix $\mathbf{S}(r, \theta, z)$ for the classical plate theory has been explicitly defined and studied in reference [23]. Hence only condensed expressions are presented here:

$$\mathbf{S}(r, \theta, z) = [S_1(r, \theta, z)\ \ S_2(r, \theta, z) \ldots S_i(r, \theta, z) \ldots S_{N_S}(r, \theta, z)], \quad (19a)$$

$$S_i(r, \theta, z) = R_k(r)\Theta_\ell(\theta), \qquad k = 0, \ldots, N_r, \qquad \ell = 0, \ldots, N_\theta, \quad (19b\text{–}d)$$

$$N_S = (N_r + 1)(N_\theta + 1), \qquad i = \ell N_r + k + 1 = 1, \ldots, N_S, \quad (19e, f)$$

where $R_k(r)$ and $\Theta_\ell(\theta)$ are defined as

$$R_k(r) = \left\{ \sum_{j=0}^{k} b_j \frac{(r - r_i)^j}{(r_o - r_i)^j} \in \mathbf{P}^k(r) : \langle R_p, R_q \rangle_r = \int_{r_i}^{r_o} R_p\, R_q\, r\, \mathrm{d}r = \delta_{pq} \right\},$$

$$p = 0, 1, \ldots, N_r, \qquad q = 0, 1, \ldots, N_r \quad (20a)$$

and

$$\Theta_\ell(\theta) = \left\{ \left\{ \begin{array}{ll} \cos\left(\dfrac{\ell}{2}\theta\right), & \text{if } \ell \text{ is even} \\ \sin\left(\dfrac{\ell+1}{2}\theta\right), & \text{if } \ell \text{ is odd,} \end{array} \right\} : \langle \Theta_f, \Theta_g \rangle_\theta = \int_0^{2\pi} \Theta_f\, \Theta_g\, \mathrm{d}\theta = \delta_{fg} \right\}, \quad (20b)$$

$$f = 0, 1, \ldots, N_\theta, \qquad g = 0, 1, \ldots, N_\theta.$$

Here $\mathbf{P}^k(r)$ is a polynomial of order k and

$$\delta_{pq} = \begin{cases} 1, \text{ if } p = q, \\ 0, \text{ if } p \neq q. \end{cases}$$

We define an inner product over the (r, θ) domain by noting that $\mathrm{d}r \perp r\,\mathrm{d}\theta$:

$$\langle S_i, S_j \rangle_{r,\theta} = \langle R_p \Theta_f, R_q \Theta_g \rangle_{r,\theta} = \langle R_p, R_q \rangle_r \langle \Theta_f, \Theta_g \rangle_\theta, \tag{21}$$
$$i = fN_r + p + 1, \qquad j = gN_r + q + 1.$$

Therefore $\{S_i\}_0^{N_S}$ is a bi-orthogonal set with respect to $\langle S_i, S_j \rangle_{r,\theta} = \int_{r_i}^{r_o} \int_0^{2\pi} S_i S_j r\,\mathrm{d}\theta\,\mathrm{d}r$. Hence,

$$\langle S_i, S_j \rangle_{r,\theta} = \langle R_p \Theta_f, R_q \Theta_g \rangle_{r,\theta} \neq 0 \text{ if } p = q \vee f = g. \tag{22}$$

Using equation (18), we obtain the following expression for mesh stiffness where offset $h^{ij}(\theta^i{*})$ and contact length $\Gamma^{ij}(\theta^i{*})$ and stiffness per unit length K^{ij} can again be obtained from the existing gear contact mechanics programs [31]:

$$\mathbf{K}_m^{ij-\ell}(\theta^i{*}) = \int_{h^{ij}(\theta^i{*}) - \Gamma^{ij}(\theta^i{*})/2}^{h^{ij}(\theta^i{*}) + \Gamma^{ij}(\theta^i{*})/2} \begin{bmatrix} \mathbf{I}{*} \\ \tilde{\mathbf{u}}_{\sigma^{ij}}^{i}(\theta^i{*}) \\ \mathbf{S}_{\sigma^{ij}}^{iT} \end{bmatrix} \hat{\mathbf{p}}_o^{ij}(\theta^i{*}) K^{ij} \hat{\mathbf{p}}_o^{ijT}(\theta^i{*}) \begin{bmatrix} \mathbf{I}{*} & \tilde{\mathbf{u}}_{\sigma^{ij}}^{\ell T}(\theta^i{*}) & \mathbf{S}_{\sigma^{ij}}^{\ell} \end{bmatrix} \mathrm{d}\sigma, \quad \ell = i, j. \tag{23}$$

The "pseudo forces" acting on gears $\mathbf{Q}_{mg}^{ij-i^*}(\Omega{*}, t)$ and $\mathbf{Q}_{mg}^{ij-j^*}(\Omega{*}, t)$ vanish due to the orthogonality condition. Therefore the rigid body and the transverse flexural motion equations are uncoupled.

4.2. REDUCED MESH EXPRESSION USING RING THEORY

The elastic deformation modes of ring gears in epicyclic trains or gears with thin flanks as shown in Figure 3(b) are similar to the radial deformation modes of a ring. Hence the modal functions of a ring [27] can be used in equation (14). The orthogonal shape function matrix $\mathbf{S}(\theta)$ for a ring are given as follows where θ is the angular position in the gear co-ordinates $\mathbf{X}_G^i - \mathbf{Y}_G^i - \mathbf{Z}_G^i$:

$$\mathbf{S}(\theta) = \begin{bmatrix} \cos(\theta) & -\sin(\theta) & 0 \\ \sin(\theta) & \cos(\theta) & 0 \\ 0 & 0 & 0 \end{bmatrix} \mathbf{S}^*(\theta), \tag{24a}$$

$$\mathbf{S}^*(\theta) = [\mathbf{S}_1(\theta)\ \mathbf{S}_2(\theta) \cdots \mathbf{S}_r(\theta) \cdots \mathbf{S}_{N_s}(\theta)]; \tag{24b}$$

$$\mathbf{S}_r(\theta) = \begin{bmatrix} C_1(\theta) & C_2(\theta) \\ C_1(\theta) & C_2(\theta) \\ 0 & 0 \end{bmatrix}, \qquad r = 0, 1, 2, \ldots, N_S. \tag{24c}$$

Here,

$$C_1(\theta) = \begin{cases} \cos\left(\dfrac{r}{2}\theta\right), & r \text{ is even}, \\ \sin\left(\dfrac{r+1}{2}\theta\right), & r \text{ is odd}, \end{cases} \qquad C_2(\theta) = \begin{cases} \sin\left(\dfrac{r}{2}\theta\right), & r \text{ is even}, \\ \cos\left(\dfrac{r+1}{2}\theta\right), & r \text{ is odd}. \end{cases} \tag{24d}$$

If the transverse modes of such gears are ignored, these equations can again be reduced to equations (18a and b) where $\mathbf{I}^* = [0\ 0\ 1]$, mesh position vectors

$$\tilde{\bar{\mathbf{u}}}^i_{\sigma^{ij}} = \begin{bmatrix} 0 & \bar{\mathbf{u}}^i_{\sigma^{ij}z} & \bar{\mathbf{u}}^i_{\sigma^{ij}y} \\ \bar{\mathbf{u}}^i_{\sigma^{ij}z} & 0 & -\bar{\mathbf{u}}^i_{\sigma^{ij}x} \end{bmatrix} \quad \text{and} \quad \tilde{\bar{\mathbf{u}}}^j_{\sigma^{ij}} = \begin{bmatrix} 0 & -\bar{\mathbf{u}}^j_{\sigma^{ij}z} & \bar{\mathbf{u}}^j_{\sigma^{ij}y} \\ \bar{\mathbf{u}}^j_{\sigma^{ij}z} & 0 & -\bar{\mathbf{u}}^j_{\sigma^{ij}x} \end{bmatrix}$$

and the generalized co-ordinates $\mathbf{q}^i_m = [\mathbf{R}^i_{Gm_z}\ q^i_{m_x}\ q^i_{m_y}\ \mathbf{q}^i_{f_m}]$ and $\mathbf{q}^j_m = [\mathbf{R}^j_{Gm_z}\ q^j_{m_x}\ q^j_{m_y}\ \mathbf{q}^j_{f_m}]$. $\mathbf{S}^i_{\sigma^{ij}}$ and $\mathbf{S}^j_{\sigma^{ij}}$ are the value of the ring shape function $\mathbf{S}(\theta)$ evaluated at σ^{ij} for gears i and j respectively. Again the "pseudo forces" acting on gears $\mathbf{Q}^{ij-i*}_{mg}(\Omega^*, t)$ and $\mathbf{Q}^{ij-j*}_{mg}(\Omega^*, t)$ vanish due to the orthogonality of the rigid body motion and the radial or circumferential flexural motion.

4.3. REDUCED MESH EXPRESSION USING NUMERICAL SHAPE FUNCTIONS

It is difficult to obtain theoretical shape functions which may accurately represent the flexural or rigid body motions of the gears which the gear-shaft sub-assemblies deviate considerably from any of the classical structural elements mentioned in the preceding sections such as the one shown in Figure 3(c). For practical systems with complicated geometry, other numerical solutions obtained from say finite element codes [31] can be used to obtain the shape functions $\mathbf{S}(r, \theta, z)$ of unassembled sub-assemblies. These can be assembled in the multi-body dynamics format to model the complete multi-mesh geared system. This modeling scheme reduces equations (14a and b) to the following where $\mathbf{q}^i_m = \mathbf{q}^i_{f_m}$ and $\mathbf{q}^j_m = \mathbf{q}^j_{f_m}$ are flexibility co-ordinates and $\mathbf{S}^i_{\sigma^{ij}}$ and $\mathbf{S}^j_{\sigma^{ij}}$ are shape function $\mathbf{S}(r, \theta, z)$ evaluated at the mesh position σ^{ij}:

$$\delta\mathbf{r}^j_{P_{\sigma^{ij}}}(t) = \mathbf{S}^i_{\sigma^{ij}}\mathbf{q}^i_m, \qquad \delta\mathbf{r}^j_{P_{\sigma^{ij}}}(t) = \mathbf{S}^j_{\sigma^{ij}}\mathbf{q}^j_m. \tag{25a, b}$$

Substituting these into equation (11), the mesh stiffness expression reduces to

$$\mathbf{K}^{ij-\ell}_m(\theta^{i*}) = \int_{h^{ij}(\theta^{i*}) - \Gamma^{ij}(\theta^{i*})/2}^{h^{ij}(\theta^{i*}) + \Gamma^{ij}(\theta^{i*})/2} \mathbf{S}^{iT}_{\sigma^{ij}}\hat{\mathbf{p}}^{ij}_o(\theta^{i*})K^{ij}\hat{\mathbf{p}}^{ijT}_o(\theta^{i*})\mathbf{S}^{\ell}_{\sigma^{ij}}\,\mathrm{d}\sigma, \quad \ell = i, j. \tag{26}$$

Additional "pseudo forces" $\mathbf{Q}^{ij-i*}_{mg}(\Omega^*, t)$ and $\mathbf{Q}^{ij-j*}_{mg}(\Omega^*, t)$ are not required here since they are implicitly embedded in equation (26).

5. OTHER SYSTEM MATRICES

5.1. STRUCTURAL STIFFNESS MATRIX OF GEAR BODY

An additional stiffness matrix $\mathbf{K}^i_{ff}(\theta^{i*})$ is needed to characterize the structural stiffness of the gear blank. Since the formulation of this matrix has already been reported by the authors in detail in reference [23], only an outline is provided here for the sake of continuity;

$$\mathbf{K}^i_{ff_{NS\times NS}} = \begin{bmatrix} 0_{3\times 3} & 0_{3\times 3} & 0_{3\times NS} \\ 0_{3\times 3} & 0_{3\times 3} & 0_{3\times NS} \\ 0_{NS\times 3} & 0_{NS\times 3} & \mathscr{K}^i_{ff_{NS\times NS}} \end{bmatrix}, \qquad \mathscr{K}^i_{ff} = \oint_{V^i} (\mathscr{D}^i\mathbf{S}^i)^T\mathbf{A}^{iT}_{ROT}\,\mathbf{E}^{iT}\mathbf{A}^i_{ROT}\,\mathscr{D}^i\mathbf{S}^i\,\mathrm{d}V. \tag{27a, b}$$

The differential operator $\mathscr{D}^i$ and the elastic stiffness $\mathbf{E}^i$ matrices for the classical thin plate theory [21] are as follows in the cylindrical co-ordinate (r, θ, z) system where E^i is the Young's modulus and v^i is Poisson's ratio of the ith gear:

$$\mathscr{D}^i = \begin{bmatrix} -z^i \dfrac{\partial^2}{\partial r^{i2}} \\ -z^i \dfrac{z^i}{r^{i2}} \dfrac{\partial^2}{\partial \theta^{i2}} - \dfrac{z^i}{r^i} \dfrac{\partial}{\partial r^i} \\ -2 \dfrac{z^i}{r^i} \dfrac{\partial^2}{\partial r^i \partial \theta^i} + 2 \dfrac{z^i}{r^{i2}} \dfrac{\partial}{\partial \theta^i} \end{bmatrix}, \qquad \mathbf{E}^i = \begin{bmatrix} \dfrac{E^i}{1-v^{i2}} & \dfrac{E^i v^i}{1-v^{i2}} & 0 \\ \dfrac{Ev}{1-v^{i2}} & \dfrac{E}{1-v^{i2}} & 0 \\ 0 & 0 & \dfrac{E^i}{2(1+v^i)} \end{bmatrix}. \quad (28, 29)$$

Here, $\mathbf{A}^i_{ROT}$ is the rotational matrix associated to the large mean rotation $\Omega^{i*}t$ about the $Z^i_{G_m}$ axis as well as the small vibratory rotational displacements θ^i_{xm}, θ^i_{ym} and θ^i_{zm}:

$$\mathbf{A}^i_{ROT}(t) = \begin{bmatrix} \cos \Omega^{i*}t & -\sin \Omega^{i*}t & 0 \\ \sin \Omega^{i*}t & \cos \Omega^{i*}t & 0 \\ 0 & 0 & 1 \end{bmatrix} \mathbf{A}^i(t). \quad (30)$$

Similar matrices can be formed if other plate theories such as Mindlin's [32] were used to model the plate out-of-plane vibration.

The structural stiffness matrix $\mathscr{K}^i_{ff}$ for a ring type gear is similar to equation (27a) with the matrix $\mathscr{K}^i_{ff}$ given as following, where $\bar{r}^i$ is the mean radius, h^i is the ring thickness, A^i is the cross-section area, I^i is the area moment of inertia, E^i is the Young's modulus and v^i is the Poisson's ratio of the ith ring gear:

$$\mathscr{K}^i_{ff} = \begin{bmatrix} \dfrac{D^i}{\bar{r}^{i4}} \dfrac{\partial^4}{\partial \theta^4} + \dfrac{\kappa}{\bar{r}^{i2}} & -\dfrac{D^i}{\bar{r}^{i4}} \dfrac{\partial^3}{\partial \theta^3} + \dfrac{\kappa^i}{\bar{r}^{i2}} \dfrac{\partial}{\partial \theta} & 0 \\ \dfrac{D^i}{\bar{r}^{i4}} \dfrac{\partial^3}{\partial \theta^3} - \dfrac{\kappa^i}{\bar{r}^{i2}} \dfrac{\partial}{\partial \theta} & -\dfrac{D^i}{\bar{r}^{i4}} \dfrac{\partial^2}{\partial \theta^2} - \dfrac{\kappa^i}{\bar{r}^{i2}} \dfrac{\partial^2}{\partial \theta^2} & 0 \\ 0 & 0 & 0 \end{bmatrix} S^*(\theta), \quad (31a)$$

$$D^i = \frac{E^i \bar{r}^{i3}}{12(1-v^2)}, \qquad \kappa^i = \frac{E^i h^i}{1-v^2}. \quad (31b, c)$$

The structural stiffness matrix $\mathbf{K}^i_{ff}$ when using external, numerically generated shape functions as described in section 3.3 is again similar to that given in equations (24). However the differential operator $\mathscr{D}^i$ and the elastic stiffness matrix $\mathbf{E}^i$ are given as

$$\mathscr{D}^i = \tfrac{1}{2} \begin{bmatrix} 2\dfrac{\partial}{\partial x} & 0 & 0 \\ 0 & 2\dfrac{\partial}{\partial y} & 0 \\ 0 & 0 & 2\dfrac{\partial}{\partial z} \\ \dfrac{\partial}{\partial y} & \dfrac{\partial}{\partial x} & 0 \\ \dfrac{\partial}{\partial z} & 0 & \dfrac{\partial}{\partial x} \\ 0 & \dfrac{\partial}{\partial z} & \dfrac{\partial}{\partial y} \end{bmatrix}, \quad (32)$$

and

$$\mathbf{E}^i = \begin{bmatrix} \frac{E^i}{1-v^{i2}} & \frac{E^i v^i}{1-v^{i2}} & \frac{E^i v^i}{1-v^{i2}} & 0 & 0 & 0 \\ \frac{E^i v^i}{1-v^{i2}} & \frac{E^i}{1-v^{i2}} & \frac{E^i v^i}{1-v^{i2}} & 0 & 0 & 0 \\ \frac{E^i v^i}{1-v^{i2}} & \frac{E^i v^i}{1-v^{i2}} & \frac{E^i}{1-v^{i2}} & 0 & 0 & 0 \\ 0 & 0 & 0 & \frac{E^i}{2(1+v^i)} & 0 & 0 \\ 0 & 0 & 0 & 0 & \frac{E^i}{2(1+v^i)} & 0 \\ 0 & 0 & 0 & 0 & 0 & \frac{E^i}{2(1+v^i)} \end{bmatrix}. \tag{33}$$

5.2. MASS MATRIX, BEARING AND SHAFT STIFFNESS AND DAMPING EXPRESSIONS

The mass matrix expressions developed in reference [9] can now be extended to include the terms arising due to the flexibility of the gear blanks [23]:

$$\mathbf{M}^i_{NS+6,NS+6}(t) = \begin{bmatrix} \mathbf{m}^i_{RR_{3\times 3}} & \mathbf{m}^i_{R\theta_{3\times 3}} & \mathbf{m}^i_{RS_{3\times NS}} \\ & \mathbf{m}^i_{\theta\theta_{3\times 3}} & \mathbf{m}^i_{\theta S_{3\times NS}} \\ \text{symm} & & \mathbf{m}^i_{SS_{NS\times NS}} \end{bmatrix}, \tag{34a}$$

$$\mathbf{m}^i_{RR_{3\times 3}}(t) = \int_{V^i} \rho^i \mathbf{I}_{3\times 3}\, \mathrm{d}V^i, \qquad \mathbf{m}^i_{R\theta_{3\times 3}}(t) = \mathbf{A}^i \int_{V^i} \rho^i \tilde{\mathbf{u}}^i_P\, \mathrm{d}V^i \mathbf{G}^i, \tag{34b, c}$$

$$\mathbf{m}^i_{RS_{3\times NS}}(t) = \mathbf{A}^i_{ROT} \int_{V^i} \rho^i \mathbf{S}^i\, \mathrm{d}V^i, \tag{34d}$$

$$\mathbf{m}^i_{\theta\theta_{3\times 3}}(t) = \mathbf{G}^{iT} \int_{V^i} \rho^i \tilde{\mathbf{u}}^i_P \mathbf{A}^{iT} \mathbf{A}^i \tilde{\mathbf{u}}^{iT}_P\, \mathrm{d}V^i \mathbf{G}^i, \qquad \mathbf{m}^i_{R\theta_{3\times NS}}(t) = \mathbf{G}^{iT} \int_{V^i} \rho^i \tilde{\mathbf{u}}^i_P \mathbf{A}^{iT} \mathbf{A}^i_{ROT} \mathbf{S}^i\, \mathrm{d}V^i, \tag{34e, f}$$

$$\mathbf{m}^i_{R\theta_{NS\times NS}}(t) = \int_{V^i} \rho^i \mathbf{S}^{iT} \mathbf{A}^{iT}_{ROT} \mathbf{A}^i_{ROT} \mathbf{S}^i\, \mathrm{d}V^i. \tag{34g}$$

The formulation of the bearing and shaft stiffness have been presented in reference [9]. Again, since the focus of this study is on the gear mesh dynamics, a similar formulation is used here but certain modifications are necessary to define the gear-shaft interface boundary conditions i.e., at the internal edge ($r = r_s$) of the flexible gear disks. Hayashi *et al*. [33, 34] have examined thick annular plates which were solidly mounted on shafts without any clamp or splines; disk and shaft were fabricated as an integral unit in their experiments. They determined the boundary conditions by assuming the shaft as a semi-infinite plate. However, it was observed that for relatively long shafts when length exceeds diameter by a ratio of 10 or more, the combined bending and torsional stiffness $\mathbf{K}^i_s$ of shafts as obtained from beam theory can be lumped with the bearing stiffness $\mathbf{K}^i_b$ as defined in reference [9]. Hence $\mathbf{K}^i_{sb}$ can be used to define more realistic boundary conditions at the inner edge of each gear disk.

A simplified expression of energy dissipation within the mesh will be employed based on the proportional viscous damping assumption:

$$\mathbf{C}_m^{ij-k}(\theta^i*) = c_d\,\mathbf{K}_m^{ij-k}(\theta^i*), \quad k = i, j; \qquad \mathbf{Q}_{md}^{ij}(t) = \mathbf{Q}_{md}^{ij-i}(t) - \mathbf{Q}_{md}^{ij-j}(t), \quad \text{(35a, b)}$$

where c_d is a damping proportionality constant, $\mathbf{Q}_{md}^{ij-i} = \mathbf{C}_m^{ij-i}\dot{\mathbf{q}}_m^i$ is the dissipative mesh force on gear i due to its own vibratory motion and $\mathbf{Q}_{md}^{ij-j} = \mathbf{C}_m^{ij-j}\dot{\mathbf{q}}_m^j$ is the dissipative force due to the vibratory motion of gear j.

6. MULTI-MESH FORMULATION FOR COMPLIANT GEARS

6.1. METHODOLOGY

The single gear mesh formulation developed in section 2.4 can now be extended to the multi-mesh geared system. As in the previous article [9], gears can either be connected through mesh and/or by a common shaft. Some of the combinations of such connections are shown in Figure 1. Figures 1(a) and (b) show systems with a single gear mesh with both the gears attached to the transmission body through shaft-bearing interfaces. Figure 1(c) shows a typical reverse-idler system with two gear meshes and three gears each attached to the transmission body through the shaft-bearing interfaces. Figure 1(d) shows a double reducer, again with two gear meshes but four gears, two of which are directly connected to the transmission body, while the other two are connected to the transmission body as well as to each other through the shaft-bearing interface. In a multi-mesh geared system, if a gear i meshes with one or more gears given as μ^i, the elastic and damping mesh forces on this gear are the sum of forces from all of the meshes μ^i:

$$\mathbf{Q}_{mg}^i(t) = \sum_{j=1}^{\mu^i} \mathbf{Q}_{mg}^{ij}(t), \qquad \mathbf{Q}_{mg}^{i*}(\Omega*, t) = \sum_{j=1}^{\mu^i} \mathbf{Q}_{mg}^{ij*}(\Omega*, t), \quad \text{(36a, b)}$$

$$\mathbf{Q}_{m\epsilon}^i(t) = \sum_{j=1}^{\mu^i} \mathbf{Q}_{m\epsilon}^{ij}(t), \qquad \mathbf{Q}_{md}^i(t) = \sum_{j=1}^{\mu^i} \mathbf{Q}_{md}^{ij}(t). \quad \text{(37c, d)}$$

Thus, the generalized forces of the multi-mesh geared system can be obtained in the vectoral form as follows where N_G is the total number of gears:

$$\mathbf{Q}_{mg} = [\mathbf{Q}_{mg}^{1T} \quad \mathbf{Q}_{mg}^{2T} \quad \cdots \quad \mathbf{Q}_{mg}^{NTG}]^T, \qquad \mathbf{Q}_{mg}^* = [\mathbf{Q}_{mg}^{1*T} \quad \mathbf{Q}_{mg}^{2*T} \quad \cdots \quad \mathbf{Q}_{mg}^{N*GT}]^T, \quad \text{(38a, b)}$$

$$\mathbf{Q}_{md} = [\mathbf{Q}_{md}^{1T} \quad \mathbf{Q}_{md}^{2T} \quad \cdots \quad \mathbf{Q}_{md}^{NTG}]^T, \qquad \mathbf{Q}_{m\epsilon} = [\mathbf{Q}_{m\epsilon}^{1T} \quad \mathbf{Q}_{m\epsilon}^{2T} \quad \cdots \quad \mathbf{Q}_{m\epsilon}^{N_G^T}]^T, \quad \text{(38c, d)}$$

$$\mathbf{q}_m = [\mathbf{q}_m^{1T} \quad \mathbf{q}_m^{2T} \quad \cdots \quad \mathbf{q}_m^{N_G^T}]^T, \qquad \mathbf{Q}_{mg}(t) = \mathbf{K}_m(\theta^j*)\mathbf{q}_m(t), \qquad \mathbf{Q}_{md}(t) = \mathbf{C}_m(\theta^j*)\dot{\mathbf{q}}_m(t). \quad \text{(38e–g)}$$

Here, the system mesh matrices $\mathbf{K}_m$ and $\mathbf{C}_m$ are given as follows where $\mathbf{K}_m^{ij-k}$ and $\mathbf{C}_m^{ij-k}$ can be obtained from equations (17), (23), (30) and (35):

$$\begin{aligned}\mathbf{K}_{m_{i,j}}(\theta^i*) &= \sum_{k\,\in\,\mu^i} \mathbf{K}_m^{ik-i}(\theta^i*), \quad \text{if } i = j,\\ &= -\mathbf{K}_m^{ij-i}(\theta^j*), \quad \text{if } i \neq j \text{ and } j \in \mu^i,\\ &= \mathbf{0}_{6\times 6}, \quad \text{if } i \neq j \text{ and } j \notin \mu^i; \qquad i, j = 1, \ldots, N_G. \end{aligned} \quad \text{(39)}$$

$$\mathbf{C}_{m_{i,j}}(\theta^i*) = \sum_{k\,\in\,\mu^i} \mathbf{C}_m^{ik-i}(\theta^j*), \quad \text{if } i = j.$$

$$\mathbf{C}_{m_{i,j}}(\theta^{i}*) = \sum_{k \in \mu^{i}} \mathbf{C}_{m}^{ik-i}(\theta^{j}*), \quad \text{if } i = j,$$

$$= -\mathbf{C}_{m}^{ij-i}(\theta^{j}*), \quad \text{if } i \neq j \text{ and } j \in \mu^{i},$$

$$= \mathbf{0}_{6\times 6}, \quad \text{if } i \neq j \text{ and } j \notin \mu^{i}; \qquad i, j = 1, \ldots, N_G. \tag{40}$$

The shaft-bearing stiffness matrix $\mathbf{K}_{sb}(\theta*)$, the structural stiffness matrix $\mathbf{K}_{ff}(\theta*)$ and the inertia matrix $\mathbf{M}$ of the complete system are obtained by assembling the individual gear-shaft sub-assembly matrices in block diagonal forms as

$$\mathbf{K}_{sb}(\theta*) = \text{diag}\,[\mathbf{K}_{sb}^{1}(\theta^{1}*) \quad \mathbf{K}_{sb}^{2}(\theta^{2}*) \quad \cdots \quad \mathbf{K}_{sb}^{N_G}(\theta^{N_G*})], \tag{41}$$

$$\mathbf{K}_{ff}(\theta*) = \text{diag}\,[\mathbf{K}_{ff}^{1}(\theta^{1*}) \quad \mathbf{K}_{ff}^{2}(\theta^{2*}) \quad \cdots \quad \mathbf{K}_{ff}^{N_G}(\theta^{N_G*})], \tag{42}$$

$$\mathbf{M} = \text{diag}\,[\mathbf{M}^{1} \quad \mathbf{M}^{2} \quad \cdots \quad \mathbf{M}^{N_G}]. \tag{43}$$

External vibratory forces are assembled as $\mathbf{Q} = [\mathbf{Q}^{1T} \ \mathbf{Q}^{2T} \ \cdots \ \mathbf{Q}^{N_G^T}]^T$ to form the external excitation vector for the system. Equations of motions for the complete multi-mesh, multi-geared system with compliant gear bodies are formed as follows by using equations (36–43). Observe the dual domain $(\theta*, t)$ characteristics of the set of linear, periodic differential equations:

$$\mathbf{M}(\theta*)\ddot{\mathbf{q}}(t) + \mathbf{C}_{m}(\theta*)\dot{\mathbf{q}}(t) + \mathbf{K}_{m}(\theta*)\mathbf{q}(t) + \mathbf{K}_{ff}(\theta*)\mathbf{q}(t) + \mathbf{K}_{sb}(\theta*)\mathbf{q}(t)$$
$$= \mathbf{Q}_{m\epsilon}(t) + \mathbf{Q}_{mg}^{*}(t) + \mathbf{Q}(t). \tag{44}$$

6.2. COMPUTATIONAL ISSUES

The dimension (d.o.f.) of equation (44) depends on the transmission system being modelled, the relative compliance and geometry of gear blanks and the frequency range of interest. If the gears are relatively rigid, the flexible co-ordinates can be eliminated altogether and then each gear-shaft sub-assembly has only 6 d.o.f. For example, configuration I of Figure 1 has 12 d.o.f. while configuration IV will have 24 d.o.f. If the gears were compliant, a large number of flexible co-ordinates $\mathbf{q}_f$ must be included in equation (44) as discussed in section 3. The number of these flexibility co-ordinates also depends on the frequency range of interest and eigensolutions of the gear blanks. For example, consider the single gear mesh assembly of configuration I again where both gears resemble an annular plate. Suppose that there are 10 gear blank modes within the frequency range of interest; at least 10 flexibility co-ordinates must be retained in each gear-shaft subassembly. This will result in an overall model with 32 d.o.f. However, this number increases significantly if one were to model the single gear mesh assembly of configuration II as shown in Figure 1. Now one gear has three circular holes within its body. The number of shape functions required to accurately represent the first 10 modes of this gear is approximately 120. As a consequence the total d.o.f. required to obtain a solution over the same frequency range will now be 142.

The issue of dimension is of little significance if only the eigensolutions of the reduced LTI models are required since the eigenvalue problem is not very computer intensive. However, if time or position varying characteristics of the system were to be retained (LTV or NLTV), one would have to employ numerical integration, multi-term harmonic balance or similar schemes [9, 39]. Since these techniques are highly computer intensive, a significant increase in dimension translates into a very high computing time. It is therefore suggested that preliminary design studies should be conducted by using the corresponding LTI model and the final analysis be carried out with a reduced order LTV or NLTV model.

TABLE 1

A summary of gear assemblies studied

Example Gear assembly no.		Two gears, single mesh I	II	III	IV	Three gears, dual mesh (reverse-idler) V	Four gears, dual mesh (double reducer) VI	Ring gears, single mesh VII
Type of gears		Spur	Helical, helix angle $\Psi = 20^\circ$			Helical, helix angle $\Psi = 20^\circ$		Spur
Gear no. 1	r_o	89·4	89·4	89·4	89·4	89·4	80·0	89·4
(mm)	r_i	19·98	19·98	19·98	19·98	19·98	19·98	83·15
	t	6·25	6·25	6·25	6·25	6·25	6·25	6·25
Gear no. 2	r_o	89·4	89·4	80·0	89·4	80·0	89·4	80·0
(mm)	r_i	19·98	19·98	19·98	19·98	19·98	19·98	73·75
	t	6·25	6·25	6·25	6·25	6·25	6·25	6·25
Gear no. 3	r_o					89·4	89·4	
(mm)	r_i	—	—	—	—	19·98	19·98	—
	t					6·25	6·25	
Gear no. 4	r_o						80·0	
(mm)	r_i	—	—	—	—	—	19·98	—
	t						6·25	
Shaft lengths (mm) (see Figure 1)		$l_1, l_2 = 200$				$l_1, l_2, l_3 = 200$	$l_1, l_4, l_{23} = 200$ $l_{21}, l_{3r} = 100$	—
Mesh parameters		Mesh stiffness/unit length, $K_m = 1{\cdot}0$ GN/m^2; contact length $\Gamma = 6{\cdot}25$ mm						$K_m = 0{\cdot}1$ GN/m^2
Type of analysis		LTI			LTI and LTV	LTI	LTI	LTI
Results		Table 2 Figures 6, 7	Table 2 Figures 6, 7, 17	Table 3, 4 Figures 3, 7, 16–18	Table 5 Figures 8, 19	Table 6 Figures 9, 20	Table 7 Figures 10	Table 8 Figure 11

Note: Gear 1 has 3 circular holes: $r_h = 55{\cdot}4$ mm, $\xi_h = 20{\cdot}0$ mm (see Figure 1).

7. MODAL STUDIES

7.1. EIGENSOLUTIONS

Equation (44) can be converted into an equivalent LTI formulation by using time (t) averaged contact length Γ^{ij} and offset parameters h^{ij}. This yields the following eigenvalue problem where $X = \mathbf{M}^{-1}(\mathbf{K}_{mo} + \mathbf{K}_{ff} + \mathbf{K}_{sb})$, ω_{nr} is the rth natural frequency, $\mathbf{q}_r$ is the rth eigenvector or mode shape, and subscript o indicates a parameter averaged about an operating point o:

$$[-\omega_{nr}^2\mathbf{I} + X]\mathbf{q}_r = \mathbf{0}. \tag{45}$$

Given the time-invariant system, a finite element model of the quasi-static system could also be constructed by using any general purpose commercial code. We have employed the ANSYS software [35] and eight noded, isoparametric brick elements are used to describe the compliant gears. The distributed gear mesh interface is simulated by creating an array of linear spring elements along the line of action. The shafts are formed from three-dimensional beam elements and the bearings are described as lumpted linear springs. The shaft is connected to the gears through rigid beam elements of zero mass. Refer to the prior article [23] for other details.

7.2. NATURAL MODES OF UNITY GEAR PAIR

The first example considered is the single spur gear pair assembly (I) with unity gear ratio ($m_g = 1$) as shown in Figure 1(a); other details can be found in Table 1. The system

TABLE 2

Natural frequencies of single mesh gear assemblies I and II as obtained from FEM and MBD formulation: *see Table* 1 *for gear specifications*

Mode r	Natural frequencies ω_{nr} (Hz) Assembly I Helix angle = 0° MBD	FEM	ϵ%†	Assembly II Helix angle = 20° MBD	FEM	ϵ%†
1	0	0	0·0	0	0	0·0
2	347	357	2·8	329	337	2·4
3	451	464	2·8	451	464	2·8
4	451	464	2·8	451	464	2·8
5	451	464	2·8	451	464	2·8
6	675	681	0·8	599	605	1·0
7	675	681	0·8	675	681	0·9
8	675	681	0·8	675	681	0·9
9	675	681	0·8	675	681	0·9
10	928	936	0·8	843	859	1·9
11	971	978	0·7	971	982	1·1
12	971	978	0·7	1048	1056	0·8
13	1264	1266	0·1	1264	1284	1·6
14	1264	1266	0·1	1264	1284	1·6
15	1264	1266	0·1	1264	1286	1·7
16	1264	1268	0·3	1388	1413	1·8
17	2380	2788	16	2380	2877	17·3
18	2380	2788	16	2380	2877	17·3
19	2380	2788	16	2380	2879	17·3
20	2380	2790	16	2430	2921	16·8

†$\epsilon\% = \frac{|\omega_{n,FEM} - \omega_{n,MBD}|}{\omega_{n,FEM}}$

parameters such as contact length are averaged over the mesh cycle so that the resulting system is position and time-invariant. Table 2 compares natural frequencies ω_{nr} obtained from the analytical MBD formulation as proposed in this paper and the FEM software ANSYS [35]. The second example is a single helical gear pair assembly (II) with helix angle $\psi_h = 20^\circ$ and $m_g = 1$ as described in Table 1. Table 2 also compared results for this case. An excellent agreement between analytical and FEM analyses is observed with error ϵ in ω_{nr} being less than 5% for the first 16 modes. However, a large error of 15% is observed at higher modes. This apparent discrepancy will be explained in the next section. Some of the pertinent mode shapes of this assembly are shown in Figures 6 and 7. The first mode of both configurations (I and II) represents the rigid body rotation ($\omega_{nr} = 0$) about the z-axis. The next four modes correspond to shaft bending as shown in Figure 6(a). Modes 6–9 depict gear rocking modes as shown in Figure 6(b). Such rigid body modes were

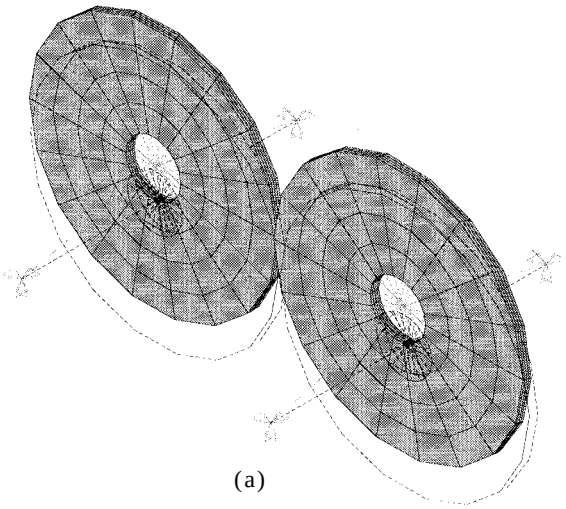

(a)

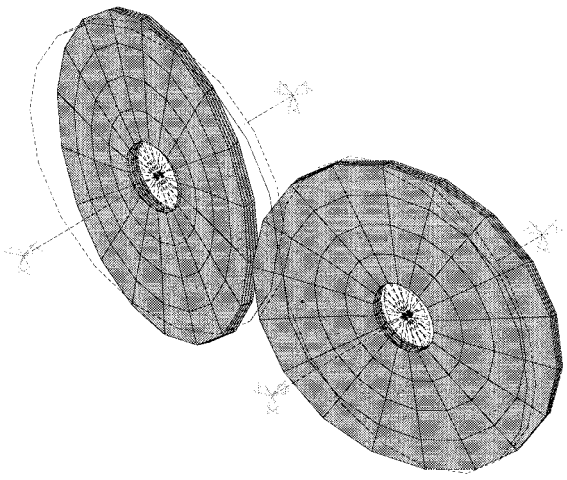

(b)

Figure 6. Rigid body deformation mode shapes of geared assembly II. (a) Mode 4, shaft bending mode; and (b) mode 7, angular rotational mode.

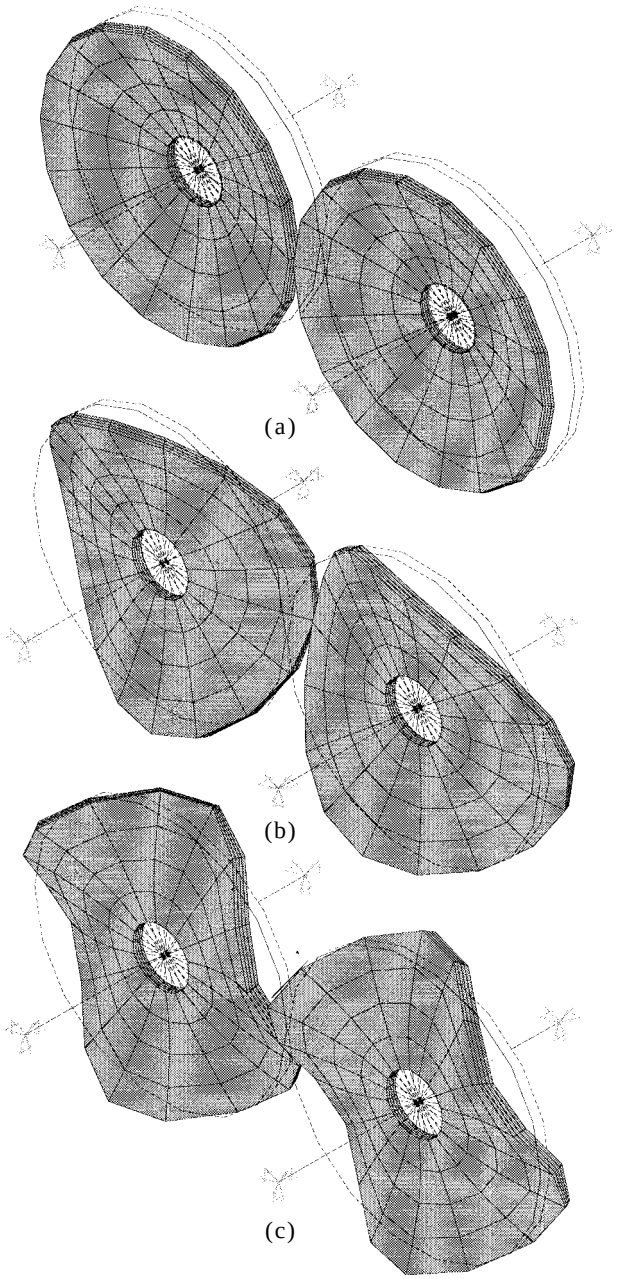

Figure 7. Flexible body mode shapes of geared assembly II. (a) Mode 11, (0, 0) flexible mode of the gears; (b) mode 13, (0, 2) flexible mode of the gears; and (c) mode 17, (0, 4) flexible mode of the gears.

obtained previously in our earlier work [9] by using rigid gears with 6 d.o.f. per gear. However, the next few modes correspond to the transverse flexibility of gear blanks themselves. Using the shape functions of section 3.1, these modes are characterized by the annular plate model notation (m, n) where m is the number of nodal circles and n is the

TABLE 3

Natural frequencies of single mesh gear assembly III as obtained from FEM and MBD formulation; see Table 1 for gear specifications

Mode	Natural frequencies ω_{nr} (Hz)				
r	MBD	FEM (coarse)	$\epsilon\%$†	FEM (refined)	$\epsilon\%$†
1	0	0	0·0	0	0·0
2	351	360	2·5	354	0·8
3	451	464	2·8	460	2·0
4	479	493	2·8	489	2·0
5	510	525	2·9	522	2·3
6	637	643	0·9	623	−2·2
7	675	681	0·9	658	−2·6
8	797	798	0·1	775	−2·8
9	904	894	−1·1	867	−3·0
10	947	953	0·6	914	−3·6
11	1057	1062	0·5	1021	−3·5
12	1264	1285	1·6	1200	−5·3
13	1297	1292	−0·4	1262	−2·8
14	1393	1380	−0·9	1325	−5·1
15	1692	1667	−1·5	1630	−3·8
16	1744	1726	−1·0	1700	−2·6
17	2380	2878	17·3	2455	3·1
18	2406	2899	17·0	2477	2·9
19	3049	3545	10	3093	1·4
20	3073	3566	13·8	3114	1·3

† $\epsilon\% = \dfrac{(\omega_{n,\mathrm{FEM}} - \omega_{n,\mathrm{MBD}})}{\omega_{n,\mathrm{FEM}}} \times 100.$

number of nodal diameters associated with each flexural mode. In some cases, only the dominant motions are labeled here. Modes 10–12 are (0, 0) type and modes 13–16 are (0, 1) type flexural modes of the gear blanks as shown in Figures 7(a) and (b) respectively. The next four modes, as shown in Figure 7(c), are associated with the (0, 2) deformation modes

TABLE 4

Description of assembly III models

Description	FEM (coarse)	FEM (refined)	Description	MBD
Number of nodes	1808	3608	Number of shape functions in radial direction	5
Number of elements	1304	2452	Number of shape functions in circumferential direction	8
Dynamic degrees of freedom	200	400	Degrees of freedom	92
Modeling time (min)	∼180	∼240	Modeling time (min)	20
CPU time (min)	18	80	CPU time (min)	7

TABLE 5

Comparison of natural frequencies of single mesh gear assembly III and its components as obtained from MBD formulation; see Table 1 for gear specifications

Mode r	Natural frequencies ω_{nr} (Hz)			
	Flexible gear-shaft sub-assemblies		Assembled systems	
	Gear no. 1	Gear no. 2	Flexible gears	Rigid gears
1	0	0	0	0
2	451	510	338	361
3	451	510	451	451
4	675	904	469	481
5	675	904	490	510
6	971	1334	606	827
7	1264	1692	668	991
8	1264	1692	670	1031
9	2380	3049	671	1096
10	2380	3049	795	1205
11			890	4729
12			1005	5528
13			1224	
14			1240	
15			1268	
16			1384	
17			2208	
18			2352	
19			2400	
20			2436	

of the gear blanks. This example clearly illustrates the simultaneous presence of both rigid body and flexible modes within the frequency range of interest.

7.3. NATURAL MODES OF A NON-UNITY HELICAL GEAR PAIR

The next example deals with a single helical gear pair with gear ratio $m_g = 0{\cdot}88$ (category III); other details can be found in Table 1. Table 3 lists the natural frequencies ω_{nr} obtained from the analytical MBD technique and from the FEM that is implemented by constructing two different models. The first "coarse" FEM model consists of 1808 nodes and 1304 elements while the second "refined" model has 3608 nodes and 2452 elements as listed in Table 4. An excellent match (with error $\epsilon < 5\%$) is again observed between analytical and "coarse" FEMs till the sixteenth mode. A relatively large discrepancy of ϵ upto 17% is observed beyond this mode. However, this apparent discrepancy vanishes when the finite element model is refined as shown in Table 3(a). Also observe that the "coarse" model appears to be more stiff than the multi-body dynamics model since mostly positive valued ϵ are found. In contrast, the "refined" model is more compliant as evident by the mostly negative values of ϵ. This observation is in agreeement with the knowledge that the numerical stiffness in finite element calculations usually decrease with an increase in dimension. Table 4 compares some of the key features of alternate modelling strategies. The multi-body dynamics scheme obviously requires at least an order of magnitude less time in terms of both system modelling and actual computations. Since the mode shapes

of this assembly are similar to the ones for assembly II (Figures 6 and 7), they are not shown.

Table 5 compares the natural frequencies of individual gear-shaft components and assemblies with rigid or flexible gears in configuration III. A large deviation in natural frequencies of the individual gear-shaft assemblies when connected together indicates that a strong coupling exists between the mesh stiffness and gear-shaft deformation modes. The angular position of the mesh with respect to the gears is fixed since this is an LTI model. Therefore those structural modes which have nodal diameters along the mesh show a weaker coupling to the mesh dynamics than the ones which have antinodes at the mesh position. This can be observed in Table 5 from a larger deviation of only one of any pairs of repeated eigenvalues. For example, the repeated ninth and tenth deformation modes of the first gear-shaft subassembly at 2380 Hz split into two distinct modes when meshed with the second gear-shaft sub-assembly. While one of the resulting natural frequencies moves down to 2352 Hz which is still close to the original frequency, the other goes down significantly to 2208 Hz.

7.4. NATURAL MODES OF A HELICAL GEAR WITH CIRCULAR HOLES

Assembly IV consists of two helical gears with three symmetric holes in the driver's web. Particulars of this gear pair are given in Table 1. Table 6 compares the natural frequencies of this system as obtained by using the MBD and FEM models. As before, the error between these two predictions is less than 3% for the first 18 modes. Note that there are fewer pairs of repeated natural frequencies for this gear pair than those observed for the symmetric pair in assembly II. This is due to the presence of three holes in the driving gear

TABLE 6

Natural frequencies of single mesh gear assembly IV as obtained from FEM and MBD formulation; *see Table* 1 *for gear specifications*

Mode r	Natural frequencies ω_{nr} (Hz)		
	MBD	FEM	$\epsilon\%$†
1	0	0	0·0
2	343	338	1·5
3	464	451	2·8
4	480	469	2·3
5	499	490	1·8
6	609	606	0·5
7	664	668	0·6
8	673	670	0·4
9	681	671	1·5
10	818	795	2·8
11	915	890	2·7
12	1016	1005	1·1
13	1160	1224	5·5
14	1213	1240	2·2
15	1267	1268	0·1
16	1381	1384	0·2
17	2173	2208	1·6
18	2306	2352	2·0
19	2789	2400	13·9
20	2813	2436	13·4

† $\epsilon\% = \frac{|\omega_{n,\mathrm{FEM}} - \omega_{n,\mathrm{MBD}}|}{\omega_{n,\mathrm{FEM}}} \times 100.$

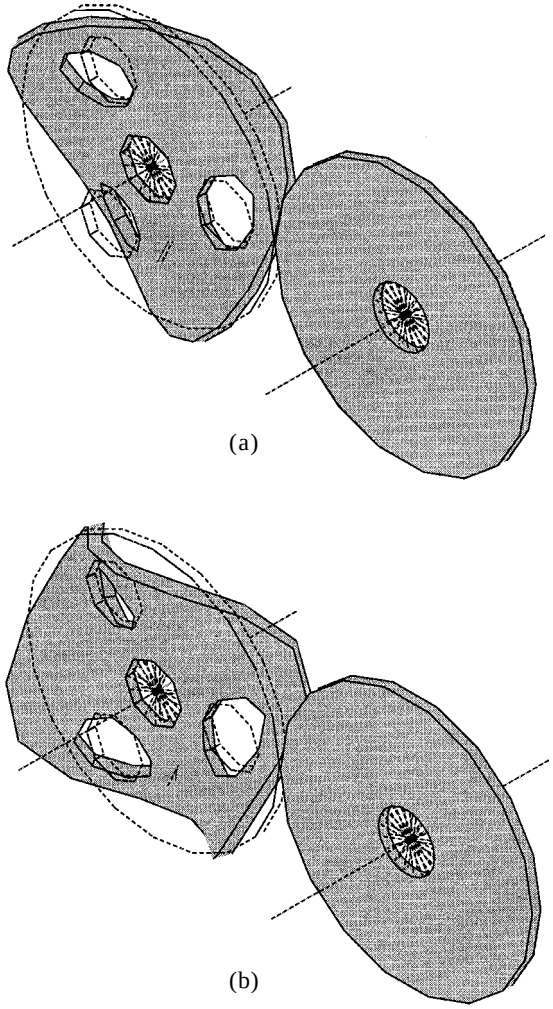

Figure 8. Mode shapes of geared assembly II. (a) Mode 13, (0, 2) flexible body mode of the driver; and (b) mode 17, (0, 4) flexible mode of the driver.

which split the repeated natural frequencies. The deformation shapes of the thirteenth and seventeenth modes associated with the (0, 2) and (0, 3) flexible body modes of the driving gear, respectively, are shown in Figures 8(a) and (b) where the (m, n) mode has m nodal diameters and n nodal circles.

7.5. NATURAL MODES OF REVERSE-IDLER REDUCER

Assembly V describes a reverse-idler reducer configuration of Table 1 with three helical gears and two meshes as shown in Figure 1(c). Both FEM and MBD predictions of natural frequencies of this assembly are given in Table 7 together with the predicted error which is less than 3% for all of the modes studied. Figures 9(a) and (b) show two selected mode shapes of this dual mesh system. The first mode shape illustrates some coupling between the rigid and flexible d.o.f. The driver and the driven gears exhibit (0, 0) flexible body modes while the idler undergoes a rigid body rotation. Due to the relatively high mesh

stiffness ($K_m = 10^8$ N/m^2), the dynamic deformations in all the gears are such that the relative motion at the mesh points on the gears is very small. This shows a strong interaction between the mesh and the structural deformation modes. The second mode shape is an example of the case where all the gears exhibit different flexible body modes. The driver and the driven gears are undergoing (0, 2) modes while the idler gear exhibits a (0, 0) mode. Notice again that the nodal diameters in the two outer gears are located such that there is a minimum possible deformation at either gear mesh interfaces.

7.6. NATURAL MODES OF A DUAL MESH SYSTEM

Now we consider a dual mesh system consisting of four spur gears in two planes, as designated by assembly IV in Figure 1, and Table 1. Table 8 compares the natural frequencies yielded by our theoretical (MBD) model with those predicted by FEM. An excellent agreement is again observed since the error is less than 3%. Mode shapes are similar to the example discussed earlier in section 7.5. Two selected bending and rocking mode shapes are shown in Figure 10.

7.7. NATURAL MODES OF RING GEARS

The next example is a gear assembly consisting of two dissimilar spur gears which resemble rings. Relevant dimensions of this assembly (VII) are given in Table 1. The transverse deformations have been artificially suppressed since this case is used to illustrate

TABLE 7

Natural frequencies of single mesh gear assembly V as obtained from FEM and MBD formulation; *see Table* 1 *for gear specifications*

Mode r	Natural frequencies ω_{nr} (Hz)		
	MBD	FEM	ϵ%†
1	0	0	0·0
2	245	241	1·6
3	419	408	2·6
4	464	451	2·8
5	464	451	2·8
6	480	467	2·7
7	525	510	2·9
8	634	632	0·3
9	645	640	0·8
10	681	675	0·9
11	681	675	0·9
12	772	772	0·0
13	864	854	1·2
14	895	904	1·0
15	966	957	0·9
16	1025	1018	0·7
17	1113	1101	1·1
18	1285	1264	1·6
19	1290	1264	2·0
20	1291	1287	0·3
21	1373	1345	2·0
22	1392	1410	1·3
23	1668	1692	1·4
24	1791	1798	0·4

† $\epsilon\% = \frac{|\omega_{n,\mathrm{FEM}} - \omega_{n,\mathrm{MBD}}|}{\omega_{n,\mathrm{FEM}}} \times 100.$

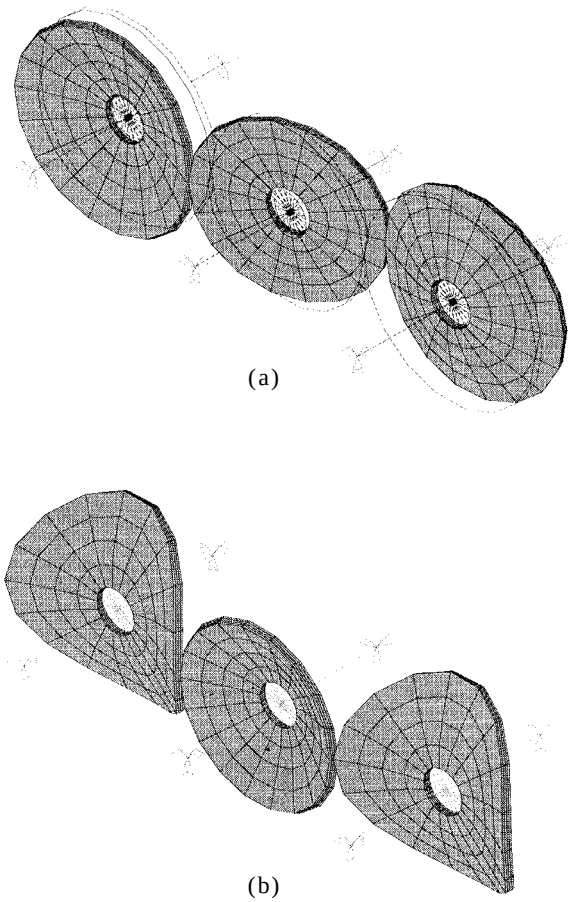

Figure 9. Mode shapes of multi-mesh geared assembly V. (a) Mode 15, coupled flexible and rigid body modes, (0, 0) flexible body mode of driver and driven gears, rotational rigid body mode of the idler; and (b) mode 20, coupled flexible body modes of the gears, (0, 2) mode of the driver and the driven gear, (0, 0) mode of the idler.

the coupling between the radial deformation motion in thin compliant gears and the gear mesh regime. Also, for the same reason, gears are free-floating, i.e., not connected to any shaft or bearings. Table 9 lists natural frequencies of individual ring gears together with those of the coupled assembly. Again, the error between the analytical (MBD) and finite element model predictions is below 3% for the first 22 modes. Figures 11(a–d) show a few mode shapes of this assembly. Unlike the previous examples, where the spur gear mesh did not result in strong coupling between the rigid body and the transverse flexural deformation modes, the radial deformation modes of the ring gears are very strongly effected by the mesh stiffness. This is obvious from a large change in natural frequencies of individual ring gears when they are meshed with each other.

8. FORCED RESPONSE STUDIES

8.1. MODAL SUPERPOSITION METHOD FOR DISK-SHAFT SUB-ASSEMBLY

Once the eigensolutions have been obtained for a disk-shaft sub-assembly, the modal superposition method can be used to calculate forced response characteristics such as

sinusoidal transfer functions. Dynamic compliance $H_{P/Q}$ and accelerance $A_{P/Q}$ between points $P(r_P, \theta_P)$ and $Q(r_Q, \theta_Q)$ on a disk-shaft subassembly are given as follows where $y_r(r_P, \theta_P)$ and $y_r(r_Q, \theta_Q)$ are the deformation of the rth mode at points P and Q (see Figure 12), ω_r and ξ_r are the rth natural frequency and modal damping ratio, respectively, and ω is the excitation frequency:

$$H_{P/Q}(\omega) = \frac{r_P}{F_Q(\omega)} = \sum_{r=1}^{N_S} \frac{y_r(r_P, \theta_P) y_r(r_Q, \theta_Q)}{(\omega_r^2 - \omega^2) + 2j\xi_r \omega\omega_r},$$

$$A_{P/Q}(\omega) = \frac{a_P}{F_Q(\omega)} = \sum_{r=1}^{N_S} \frac{-y_r(r_P, \theta_P) y_r(r_Q, \theta_Q)}{\omega^2((\omega_r^2 - \omega^2) + 2j\xi_r \omega\omega_r)}. \quad (46a, b)$$

Here, r_P and a_P are dynamic displacement and acceleration respectively at point P due to a sinusoidal force F_Q applied at point Q. The series can be truncated to N_S modes depending on the frequency range of interest.

TABLE 8

Natural frequencies of single mesh gear assembly VI as obtained from FEM and MBD formulation; *see Table* 1 *for gear specifications*

Mode r	Natural frequencies ω_{nr} (Hz)		
	MBD	FEM	$\epsilon\%$†
1	0	0	0·0
2	159	155	2·5
3	198	190	0·0
4	284	275	3·2
5	429	416	3·0
6	479	466	2·7
7	526	510	3·0
8	526	510	3·0
9	604	608	0·7
10	617	610	1·1
11	673	704	6·0
12	677	707	4·0
13	834	855	2·5
14	893	904	1·2
15	893	904	1·2
16	894	904	1·1
17	894	904	1·1
18	963	928	3·6
19	968	953	1·5
20	981	968	1·3
21	1008	997	1·1
22	1118	1073	0·0
23	1264	1264	0·0
24	1264	1264	0·0
25	1265	1264	0·1
26	1265	1264	0·1
27	1290	1334	3·4
28	1291	1334	3·3
29	1647	1692	2·7
30	1648	1692	2·7

† $\epsilon\% = \frac{|\omega_{n,\mathrm{FEM}} - \omega_{n,\mathrm{MBD}}|}{\omega_{n,\mathrm{FEM}}} \times 100.$

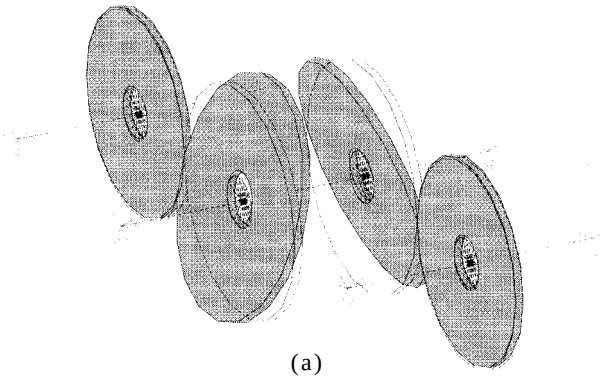

(a)

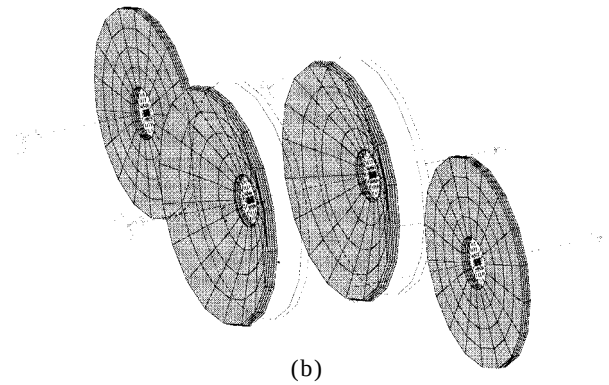

(b)

Figure 10. Mode shapes of multi-mesh geared assembly VI. (a) Mode 11, rotational rigid body modes of the first stage driver and second stage driven gears; and (b) mode 18, flexible body modes (0, 0) of the first stage driver and the second stage driven gears.

8.2. EXPERIMENTAL STUDY OF GEAR-SHAFT SUB-ASSEMBLY

An experimental clamp was built to simulate the gear-shaft interface at the inner edge (r_i) of annular gear-like disks as shown in Figure 12. The characteristics of this clamp-disk assembly is described by the authors in reference [23]. An electrodynamic shaker (5-lb force) was attached at point Q and an accelerometer at P to obtain the cross-point and driving point accelerances. The dimensions and other relevant data of several annular-like disks used in this study are given in Table 10. Figures 13–15 show the measured accelerances. In particular, Figure 13(a) compares the experimental with the analytical driving point accelerance ($A_{Q/Q}$) obtained by using equation (31b) for the annular-like disk no. 1. This resembles an annular plate. Experimental values of damping ratios were used in the analytical formulation. Predicted and experimental accelerance transfer functions compare well. Next, the accelerometer was located at point P (Figure 12) to obtain the cross-point accelerance which is shown in Figure 13(b). Again, the overall characteristics of two accelerance plots are similar except between 1000 and 1700 Hz where the experimental data has several resonance peaks that are not predicted by the modal superposition method. In reference [23], it has been shown that this clamp, like any other real life clamping condition, does not act as a perfectly rigid support, but has some dynamic characteristics of its own which couple with those of the disk. These may be

observed as extraneous peaks in the cross-point accelerance plots. The driving-point and cross-point accelerance for disk no. 2 (Table 9) are given in Figures 14(a) and (b). This disk has two circular concentric holes which makes the disk more compliant. This is evident from the higher accelerance amplitudes at the resonant peaks. Also, more effects of the clamp dynamics are observed between 1000 and 1700 Hz. Disk no. 3 has three symmetrically placed concentric holes and results are given in Figure 15. The predicted accelerance for this disk compares well with the experimental data only in the lower frequency regime. But there are considerable discrepancies between theory and experiment for the accelerance amplitude above 1000 Hz. These results suggest that the theoretical shape functions used to describe the disk are not adequate for a disk of complex geometry and cannot be subsequently used in equation (44) for obtaining the overall multi-mesh solution. For systems containing gears with such complex blank geometry, the formulation proposed in section 3 should be used instead, with experimentally obtained shape functions.

8.3. MODAL SUPERPOSITION METHOD FOR MULTI-MESH GEARED SYSTEMS

The methodology of section 5.1 for gear-shaft sub-systems is now extended to multi-mesh systems. It should however be noted that mode shapes and natural frequencies can only be obtained for the reduced LTI multi-mesh formulation of equation (45), and hence the modal superposition method is applicable only to this particular case. On

TABLE 9

Natural frequencies of single mesh ring gear assembly VII as obtained from FEM and MBD formulation; *see Table* 1 *for gear specifications*

	Natural frequencies ω_n (Hz)				
	Sub-assemblies		Assembly		
Mode r	Ring gear 1 (MBD)	Ring gear 2 (MBD)	MBD	FEM	ϵ%†
1	0	0	0	0	0·0
2	538	687	460	468	1·7
3	538	687	538	539	0·2
4	1522	1943	601	616	2·5
5	1522	1943	687	688	0·1
6	2918	3725	793	799	0·8
7	2918	3725	1522	1527	0·3
8	4719	6025	1540	1538	0·1
9	4719	6025	1943	1947	0·2
10	6922	8838	1958	1956	0·1
11	6922	8838	2918	2932	0·5
12			2925	2936	0·4
13			3725	3733	0·2
14			3731	3737	0·2
15			4719	4752	0·7
16			4723	4754	0·7
17			6025	6039	0·2
18			6028	6041	0·2
19			6922	6990	1·0
20			6925	6991	1·0
21			8838	8867	0·3
22			8840	8870	0·3

† $\epsilon\% = \frac{|\omega_{n,\mathrm{FEM}} - \omega_{n,\mathrm{MBD}}|}{\omega_{n,\mathrm{FEM}}} \times 100.$

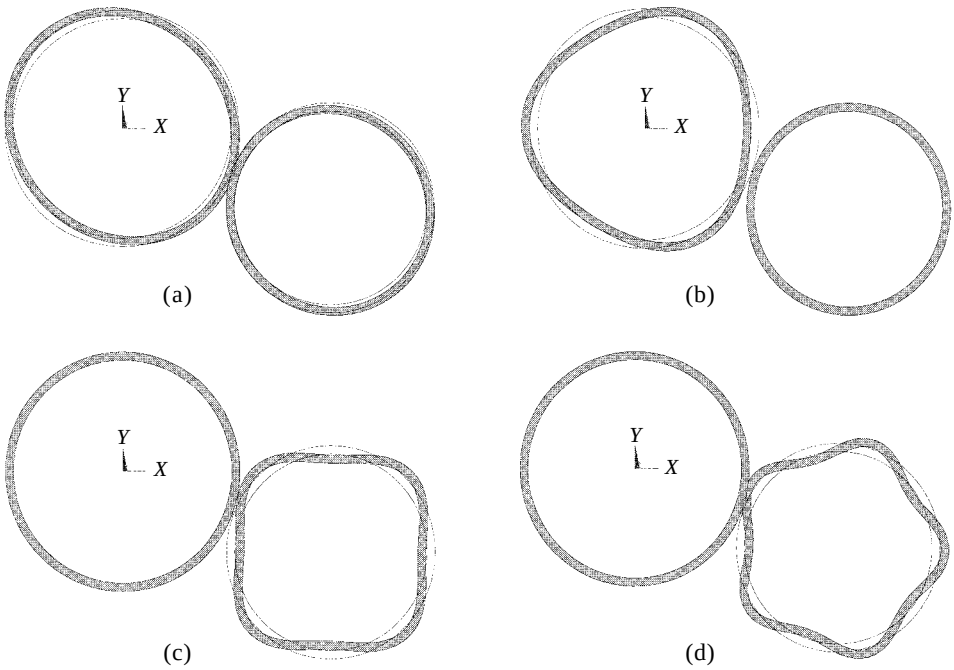

Figure 11. Mode shapes of ring gear assembly VII. (a) Mode 6, flexible body mode (2) of the driver; (b) mode 11, flexible body mode (3) of the driver; (c) mode 17, flexible body mode (4) of the driven gear; and (d) mode 21, flexible body mode (5) of the driven gear.

applying the normal mode expansion technique to equation (45), we obtain the following steady state response at frequency ω where $\mathbf{r}_P^i$ and $\mathbf{a}_P^i$ are the vectoral deformation and acceleration at point P on the ith gear while $\mathbf{F}_Q^j$ is the vectoral force at point Q on the jth gear:

$$\mathbf{u}_P^i(\omega) = [\mathbf{I}^* \quad \tilde{\mathbf{u}}_P^i \quad \mathbf{S}_P^i] \sum_{r=1}^{\infty} \left\{ \frac{y_r\, y_r^T}{(\omega_r^2 - \omega^2) + 2j\xi_r\, \omega\omega_r} \right\} \begin{bmatrix} \mathbf{I}^{*T} \\ \tilde{\mathbf{u}}_Q^{iT} \\ \mathbf{S}_Q^{jT} \end{bmatrix} \mathbf{F}_Q^j(\omega), \tag{47a}$$

$$\mathbf{a}_P^i(\omega) = [\mathbf{I}^* \quad \tilde{\mathbf{u}}_P^i \quad \mathbf{S}_P^i] \sum_{r=1}^{\infty} \left\{ \frac{-y_r\, y_r^T}{\omega^2((\omega_r^2 - \omega^2) + 2j\xi_r\, \omega\omega_r)} \right\} \begin{bmatrix} \mathbf{I}^{*T} \\ \tilde{\mathbf{u}}_Q^{iT} \\ \mathbf{S}_Q^{iT} \end{bmatrix} \mathbf{F}_Q^j(\omega). \tag{47b}$$

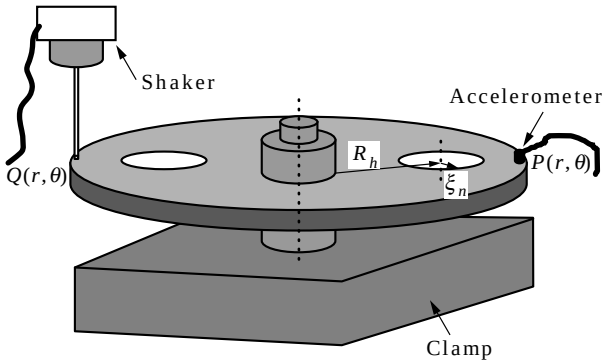

Figure 12. Schematic of experiment used for the forced response study.

TABLE 10

Annular-like disk cases used for forced response studies

Example case	Description	Pertinent dimensions (mm)
1	Annular disk with no holes	—
2	Annular disk with 2 holes	$r_h = 55{\cdot}9$, $\xi = 27$
3	Annular disk with 3 holes	$r_h = 55{\cdot}9$, $\xi = 20{\cdot}0$

$r_o = 89{\cdot}4$ mm, $r_i = 19{\cdot}98$ mm, $t = 6{\cdot}35$ mm, $E = 201$ Gpa, $\rho = 7800$ kg/m^3 and $\nu = 0{\cdot}28$. A shaft is attached to these disks at r_i.

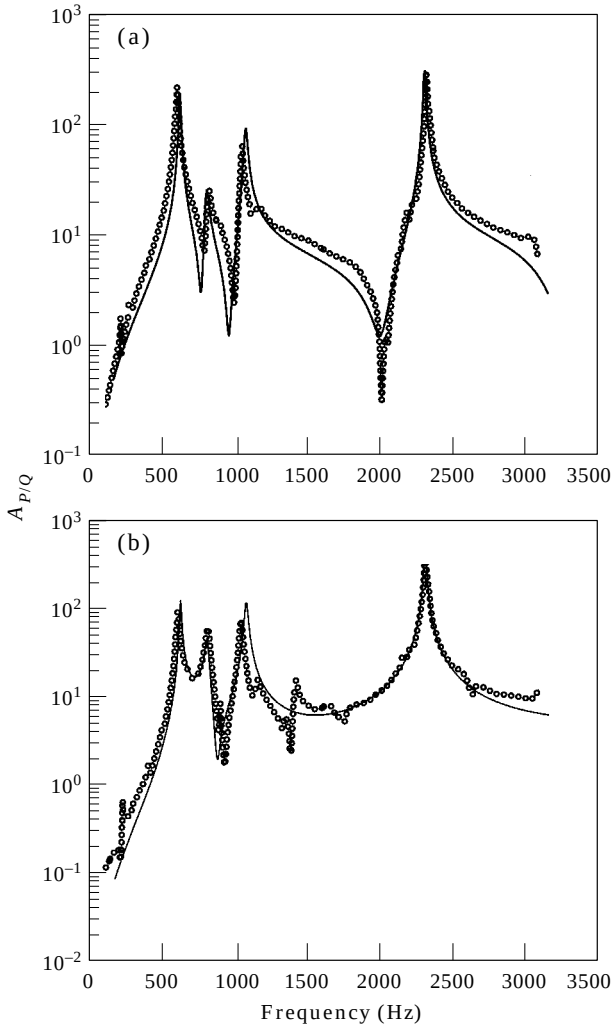

Figure 13. Forced response characteristics of gear blank no. 1. (a) Driving point acclerance $A_{Q/Q}$ spectra; and (b) cross-point accelerance $A_{P/Q}$ spectra. ——, analytical (MBD); ○, experimental.

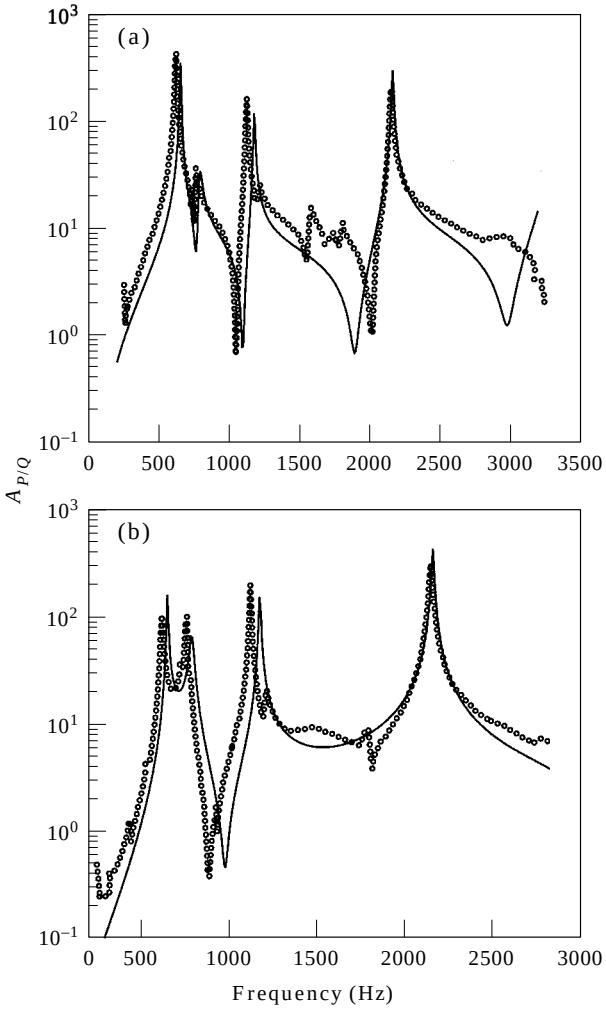

Figure 14. Comparison of forced response characteristics of gear blank no. 2 (with two circular holes). (a) Driving point accelerance $A_{Q/Q}$ spectra; and (b) cross-point accelerance $A_{P/Q}$ spectra. ——, analytical (MBD); ○, experimental.

Here, $\mathbf{I}^*$, $\tilde{\mathbf{u}}_P^i$ and $\mathbf{S}_P^i$ are as defined in section 4, ψ_r is the eigenvector matrix obtained from equation (30), ω_r is the rth natural frequency and ω is the excitation frequency. Dynamic compliance $H_{P/Q_{mn}}^{ij}$ or accelerance $A_{P/Q_{mn}}^{ij}$ transfer functions can be obtained between any of the three components ($m = x, y, z$) of response $\mathbf{r}_P^i$ or $\mathbf{a}_P^i$ respectively and any ($n = x, y, z$) component of the force $\mathbf{F}_q^j$.

8.4. STUDY OF MULTI-MESH SYSTEMS

The gear assemblies of Figure 1 and Table 1 are now studied using the forced response formulation derived in section 8.3 to better understand their dynamic behavior. Eigensolutions of these systems, as discussed in section 4, are used in equation (47b) to obtain their accelerance characteristics. Finite element models are again used to verify the forced response calculations for the reduced LTI formulation. A helical, asymmetric gear assembly (III) is chosen as an example for illustrating the dynamics of single mesh systems. Figure 16 shows good agreement between analytically obtained cross-point accelerance

$A^{12}_{P/Q_{zz}}$ and finite element predictions. Here, the excitation point $P(r = r_o, \theta = 180^\circ)$ lies on gear 1 while the response position $Q(r = r_o, \theta = 0^\circ)$ is across the mesh on gear 2. To illustrate the effect of asymmetry on the dynamics of gear pair, Figure 17 compares cross-point accelerance $A^{12}_{P/Q_{zz}}$ of this assembly with the results of a symmetric assembly (II). The asymmetric gear pair has more resonant peaks than the symmetric pair because the latter has a number of repeated natural frequencies (refer to Tables 2, 3 and 4).

Figure 18 illustrates the coupling between the rigid body and the flexible body modes via accelerance plots $A^{11}_{P/Q_{zz}}$ and $A^{22}_{P/Q_{zz}}$ for two gear-shaft sub-assemblies. Before these sub-assemblies are meshed, the resonant peaks in accelerance plots corresponded to the shaft bending and gear blank deformation modes. Further, since these gears are not similar, they have resonant peaks at different frequencies as evident from Table 5. In Figure 18, the accelerance $A^{12}_{P/Q_{zz}}$ plot for an assembly with artificially rigid gears has resonant peaks corresponding to the shaft/bearing deformation modes only. The complete assembly with compliant gears shows, however, a rather strong coupling between these

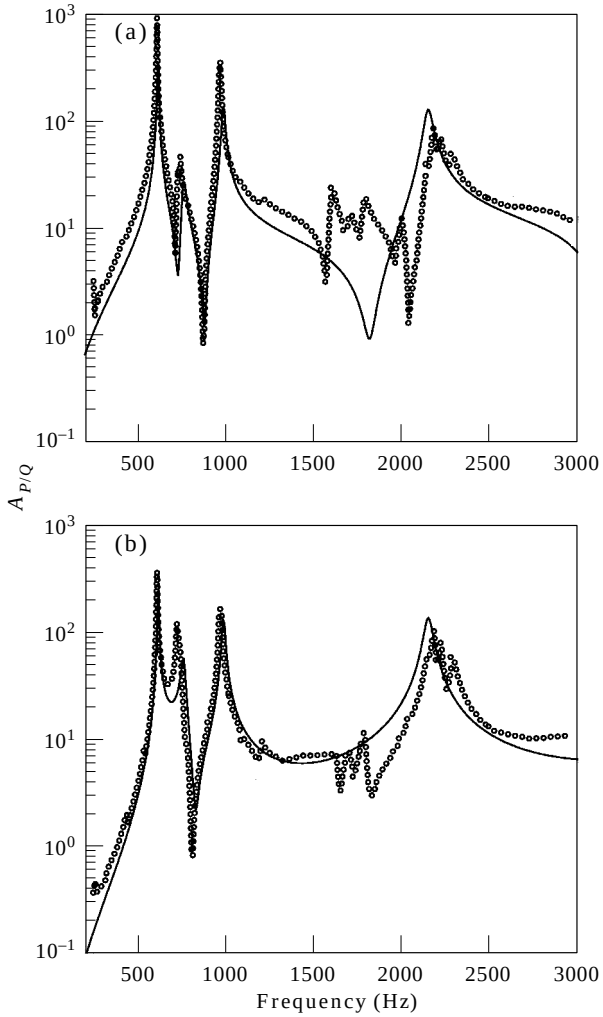

Figure 15. Forced response characteristics of gear blank no. 3 (with three circular holes). (a) Driving point accelerance $A_{Q/Q}$ spectra; and (b) cross-point accelerance $A_{P/Q}$ spectra. ——, analytical (MBD); ○, experimental.

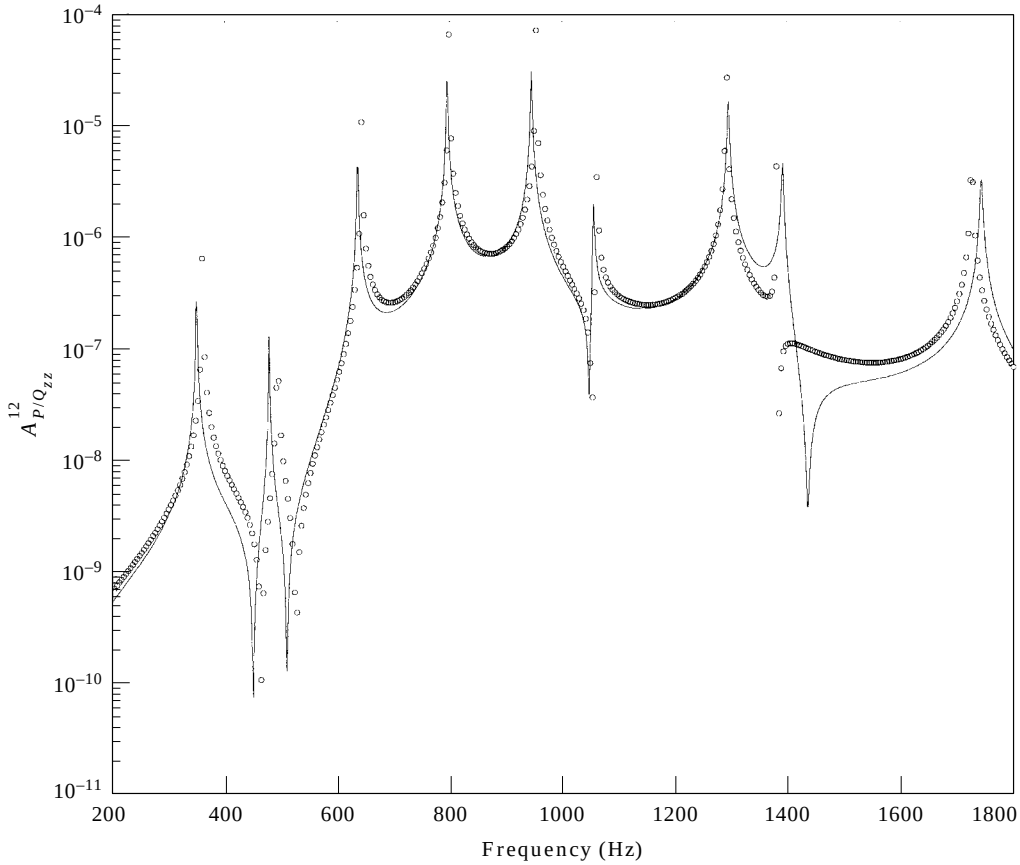

Figure 16. Cross-point accelerance $A^{12}_{P/Q_{zz}}$ spectra of gear assembly III. ——, analytical (MBD); ○, FEM.

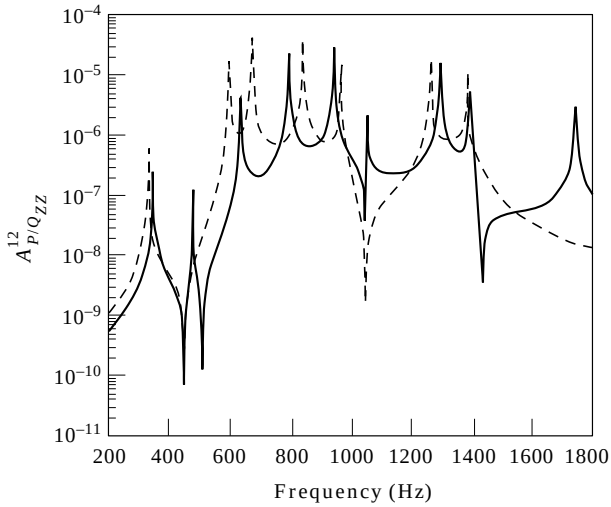

Figure 17. Cross-point accelerance $A^{12}_{P/Q_{zz}}$ spectra of (II) and asymmetric (III) gear assemblies. ——, assembly III; -----, assembly II.

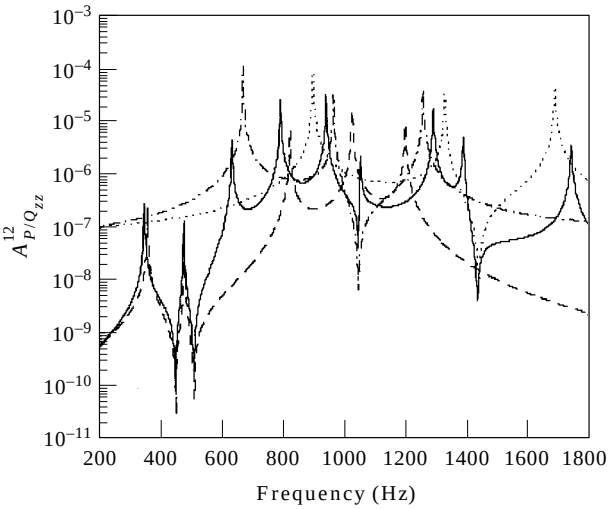

Figure 18. Cross-point accelerance of gear assembly (III) and its sub-assemblies (see Table 4). ——, $A^{12}_{P/Q_{zz}}$ spectra of assembly with flexible gears; -----, $A^{12}_{P/Q_{zz}}$ spectra of assembly with rigid gears; - · - · - · -, $A_{P/Q_{zz}}$ spectra of gear-shaft sub-assembly no. 1; · · · · · ·, $A_{P/Q_{zz}}$ spectra of gear-shaft sub-assembly no. 2.

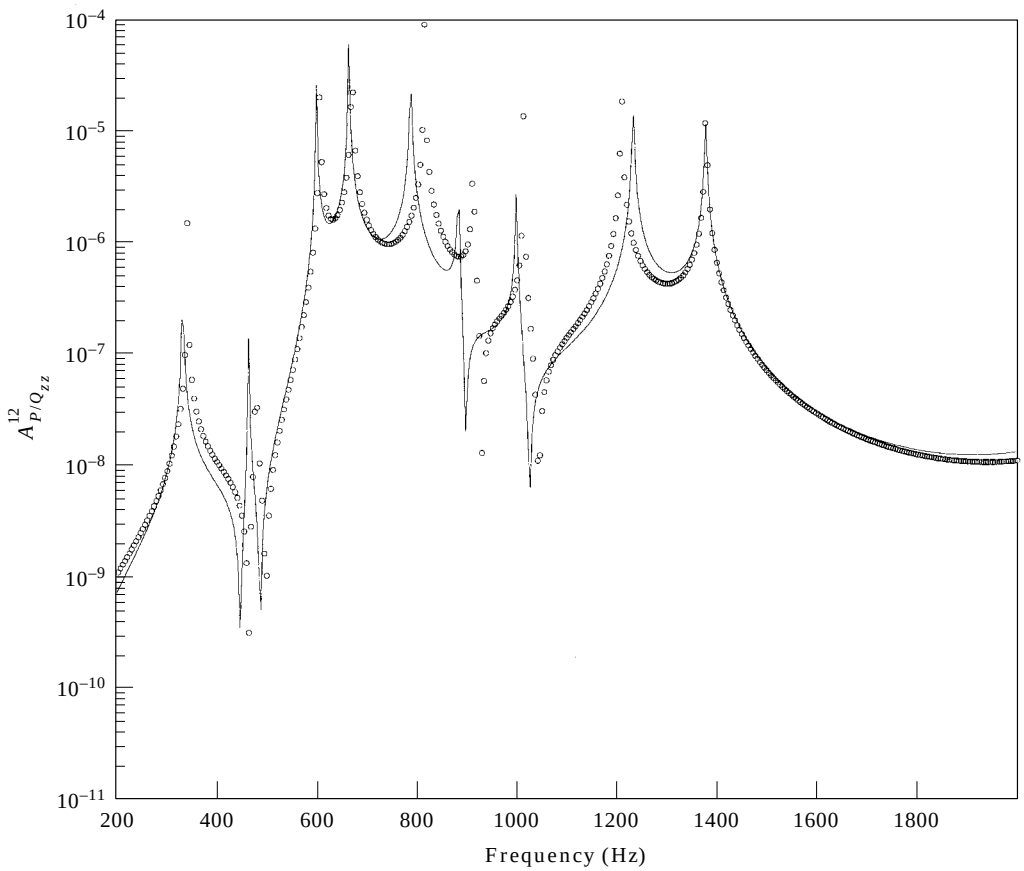

Figure 19. Cross-point accelerance $A^{12}_{P/Q_{zz}}$ spectra of gear assembly (IV). ——, analytical (MBD); ○, FEM.

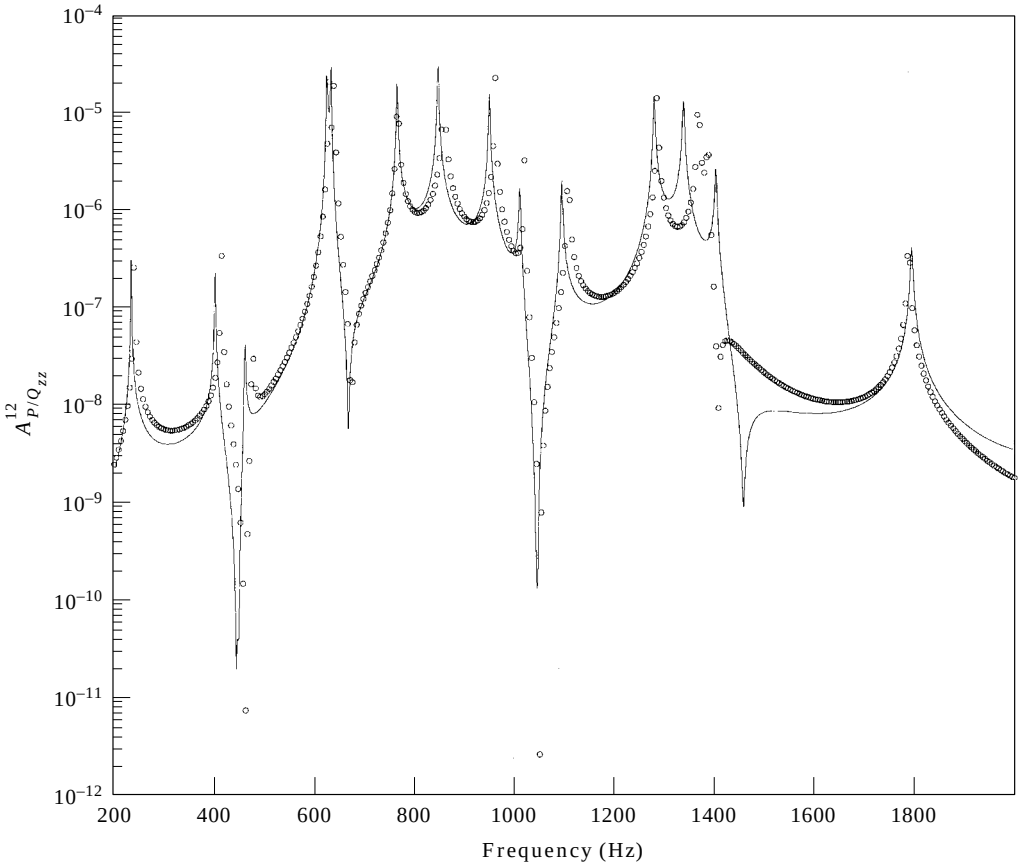

Figure 20. Cross-point accelerance $A^{12}_{P/Q_{zz}}$ spectra of gear assembly (V). ——, analytical (MBD); ○, FEM.

modes of deformation as evident from the characteristics of its accelerance as seen in Figure 18. The lower two modes correspond to rigid body rotation along the z-axis and hence they are not affected by the transverse flexural deformation of gears. But all of the higher modes deviate considerably from the sub-assembly modes due to the meshing of gears. This demonstrates the necessity of analyzing the multi-mesh geared transmission from a dynamic system viewpoint.

Gear assembly IV represents a system with a compliant, weight-optimized gear, i.e., gear no. 1 has three circular holes. The analytical formulation of section 8.3 is used to obtain the cross-point accelerance $A^{12}_{P/Q_{zz}}$ for this assembly. Figure 19 compares results with those obtained using the finite element model. Two methods predict very similar accelerance spectra, however, a slight error is observed due to the shape function approximations associated with the multi-body dynamics technique.

Finally, the gear assembly V is studied as an example of a multi-mesh geared system. Cross-point accelerance $A^{13}_{P/Q_{zz}}$ is obtained between the forcing point $P(r = r_o, \theta = 180^\circ)$ on gear 1 and the response point $Q(r = r_o, \theta = 0^\circ)$ on gear 3. Figure 20 shows a typical spectrum which is influenced by the flexible body modes of the gears and the two mesh deformations. Again a very close match is obtained between analytical (MBD) and finite element methods.

9. EFFECT OF GEAR ORIENTATION

The deformation shape functions of any gear, say i, are defined in the gear co-ordinate system X_G^i–Y_G^i–Z_G^i which rotates with respect to the mesh co-ordinate system X_{Gm}^i–Y_{Gm}^i–Z_{Gm}^i with a mean gear rotational velocity Ω^{i*}. Thus the gear body deformation shape functions rotate with respect to the stationary mesh with the same rotational velocity Ω^*. Since there is a strong coupling between the rigid body mesh dynamics and the gear body flexural dynamics, this relative rotation should give rise to "pseudo" forces $\mathbf{Q}_{mg}^{ij-j*}(\Omega^*, t)$ and $\mathbf{Q}_{mg}^{ij-i*}(\Omega^*, t)$ as discussed earlier in section 3. This effect may be easily observed by comparing the forced responses for an LTI geared assembly but evaluated at selected spatial operating points given by the rotational position $\theta^* = \int_0^t \Omega^* \, \mathrm{d}t$. Assembly IV is chosen as an example to illustrate this phenomenon since the rotational position of the gears are uniquely identified with respect to the holes in the first gear as shown in Figure 21. Due to the symmetry of the holes only three intermediate anti-clockwise rotational positions, $\theta^* = 0$, 30 and 60°, are adequate to represent the various orientations of the gears. Figure 22 shows the cross-point accelerance $A_{P_j Q_{zz}}^{12}$ spectra at three different spatial positions. The first few modes which are predominantly rigid body modes are virtually unchanged but the higher modes, corresponding to the flexible gear body modes, are strongly affected by a change in the gear orientation. Figure 22(b) shows an expanded view of the resonance peaks corresponding to the (0, 2) flexible body modes of the two gears. The first peak is due to the flexible body mode of the driver gear which has three holes within its body. As the gears rotate through 60°, there is a considerable shift in the frequency of this resonance ($\sim$50 Hz). This is because the local stiffness of the gear increases as the hole moves away from the meshing zone (refer to Figure 21), thereby resulting in a corresponding increase in the frequency associated with this resonance. The second peak however is due to the driven gear which resembles an annular disk. Since there is no change in the "local" stiffness of the driven disk with respect to the mesh as both gears rotate, no appreciable deviation in the resonant frequency is observed. This parametric coupling phenomenon can be very easily studied by the proposed multi-body

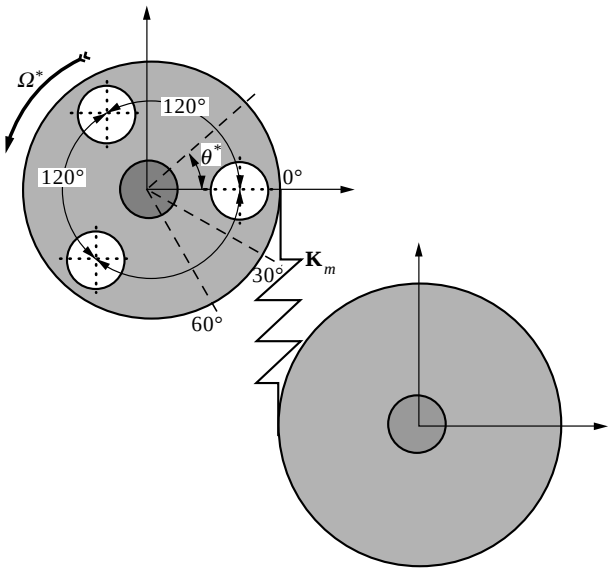

Figure 21. Different orientations of a gear assembly (III).

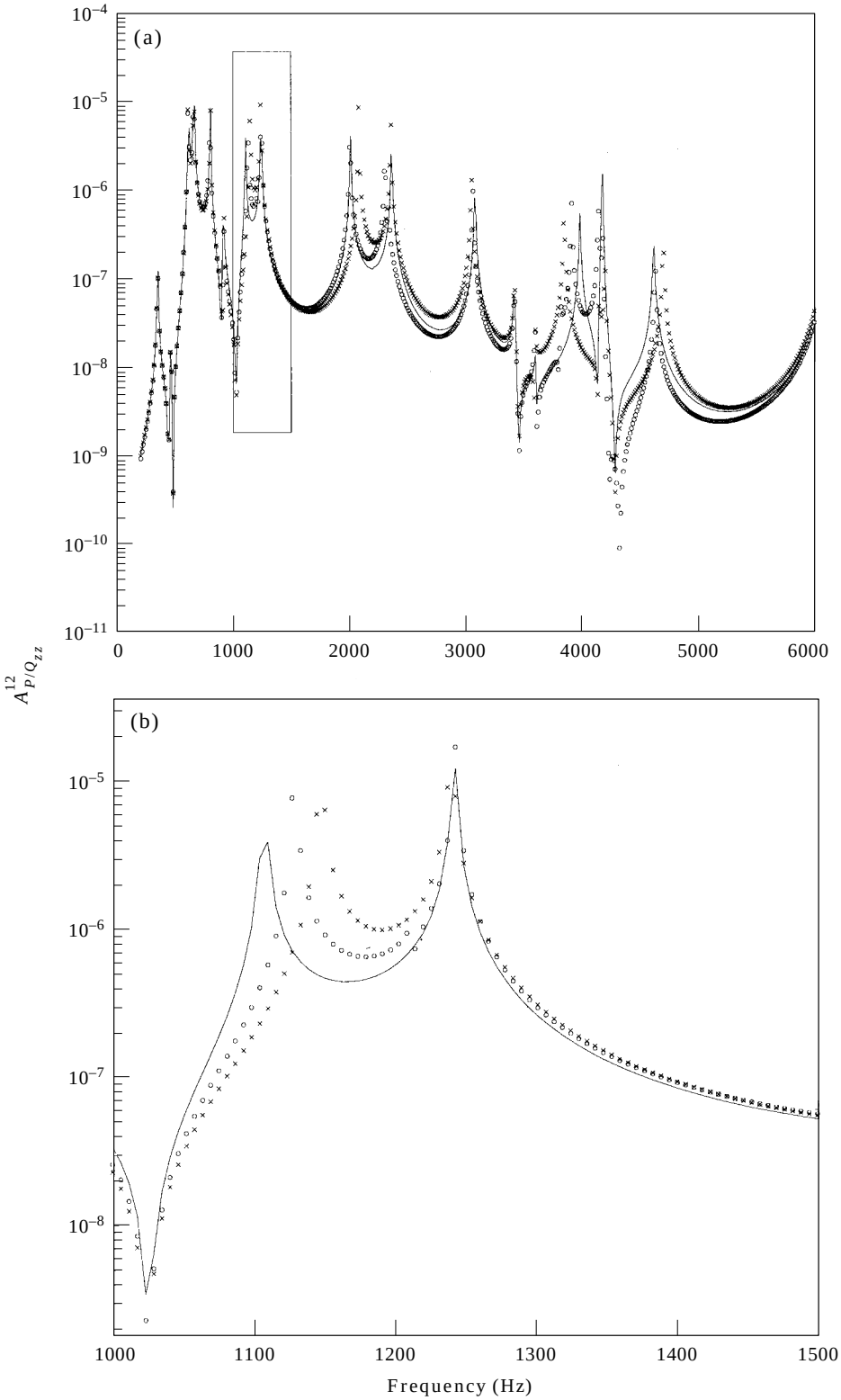

Figure 22. Cross-point accelerance $A^{12}_{P/Q_{zz}}$ spectra of gear assembly (III) at different gear orientation. (a) The complete spectra; and (b) expanded view of inset in (a) ——, $\theta^* = 0^\circ$; ○, $\theta^* = 30^\circ$; ×, $\theta^* = 60^\circ$.

dynamics methodology, unlike other numerical techniques such as finite elements. However, this is beyond the scope of this study.

10. CONCLUSION

The analysis of multi-mesh transmissions with compliant gears includes the effects of contact mechanics, rigid body gear mesh interface dynamics and their interactions with elastic deformations of gear bodies. The resulting formulation is a non-linear, spatially or time-varying system. The solution of governing equations can be obtained from the direct time domain integration, the Galerkin's procedure or other numerical techniques. However these methods are computationally intensive since a very high number of d.o.f. is involved in the computation. A reduction to a corresponding LTV equation makes the solution procedure slightly more convenient. Finally, an LTI approximation results in an eigenvalue problem that can be easily solved and compared with other LTI analyses such as the finite element method.

This paper extends the prior two articles by the same authors [9, 23] which analyzed the multi-mesh transmissions with rigid gears and compliant gear-like disks separately. Three main contributions emerge from this paper. First, a new mesh expression has been developed for gear pairs with compliant gear bodies. The dynamics of this system has been compared to the one with rigid gears, and the importance of coupling between the rigid body and flexible body dynamics has been quantified. Second, this formulation has been integrated within the multi-body dynamics framework in order to obtain a comprehensive model of a multi-mesh geared system with compliant gears. The resulting NLTV equations have been reduced to LTV and LTI equations. The importance of the time-varing characteristics of such geared systems with compliant gears has been noted. A strategy has been formulated through which shape functions from plate or ring-like bodies can be incorporated in addition to numerical eigensolutions from FEM for complex gear bodies. Third, a method of constructing forced response solutions for an LTI system has been formulated and the results compare well with finite element models. The proposed formulation reduces large degree-of-freedom spatial domain models (e.g. finite element models) to a reduced degree-of-freedom modal domain model while maintaining the accuracy of solution. This typically results in a vast improvement in solution time. Even for an LTI system the proposed method takes an order-of-magnitude less solution time than the finite element method, as evident from Table 4. This solution efficiency will increase many folds when solutions to NLTV systems are sought. Limited experimental verification of the forced response characteristics of a few individual gear-shaft sub-assemblies has been completed. Eventually, a full scale experimental study of multi-mesh geared systems with compliant gears will be required to validate the theory presented in this paper.

ACKNOWLEDGMENT

This research has been supported by the Army Research Office (URI Grant DAAL 03-92-G-0120; 1992–97. Project monitor: Dr T. L. Doligalski).

REFERENCES

1. S. Oda, T. Koide and K. Miyachika 1985 *Bulletin of the Japanese Society of Mechanical Engineers* **28**, 2434–2441. Dynamic behavior of thin-rimmed helical gears with various web arrangements.

2. N. Iwatsuki, I. Hayashi and H. Maki 1991 *Japanese Society of Mechanical Engineers International Conference on Motion and Power Transmissions*, *Hiroshima*, *Japan*, 49–53. Estimation of noise power radiation from gear bodies.
3. G. Cornejo and A. K. Rakhit 1996 *American Society of Mechanical Engineers* **DE 88**, 195–203. Identification of spiking vibrations in gears and their effect on the performance of gearbox in high speed applications.
4. H. Okamura, Y. Suzuki and N. Nakano 1996 *American Society of Mechanical Engineers* **DE 88**, 345–354. Experiments and analysis of sound-damping rings for gears: application of snap rings.
5. H. Ozguven and D. R. Houser 1988 *Journal of Sound and Vibration* **121**, 83–411. Mathematical models used in gear dynamics—a review.
6. G. W. Blankenship and R. Singh 1992 *American Society of Mechanical Engineers*, *Proceedings of the Sixth International Power Transmission and Gearing Conference* **DE 43**, 137–146. A comparative study of selected gear mesh interface dynamic models.
7. H. Iida, A. Tamura and H. Yamamoto 1986 *Bulletin of Japanese Society of Mechanical Engineers* **29**, 1811–1816. Dynamic characteristics of a gear train system with softly supported shafts.
8. G. W. Blankenship and R. Singh 1995 *Mechanism and Machine Theory* **30**, 43–57. A new gear mesh interface dynamic model to predict multi-dimensional force coupling and excitation.
9. H. Vinayak, C. Padmanabhan and R. Singh 1995 *Journal of Sound and Vibration* **185**, 1–32. Dynamic analysis of multi-mesh transmissions containing external, rigid gears.
10. P. Velex and L. Flamand 1996 *Journal of Mechanical Design* **118**, 7–14. Dynamic response of planetary trains to mesh parametric excitations.
11. F. M. L. Amirouche, N. H. Shareef and M. Xie 1991 *Machinery Dynamics and Element Vibrations* **DE 36**, 257–262. Dynamic analysis of flexible gear trains/transmissions: an automated approach.
12. F. M. L. Amirouche 1992 *Computational Methods in Multibody Dynamics*. Englewood Cliffs, NJ: Prentice Hall.
13. T. R. Kane and D. A. Levinson 1983 *Journal of Applied Mechanics* **50**, 1071–1079. Multibody dynamics.
14. A. A. Shabana 1985 *American Society of Mechanical Engineers*, *Journal of Vibration*, *Acoustics*, *Stress*, *and Reliability in Design* **107**, 431–439. Automated analysis of constrained systems of rigid and flexible bodies.
15. A. A. Shabana 1986 *Computer Methods in Applied Mechanics and Engineering* **54**, 75–91. Transient analysis of flexible multi-body systems. Part I: dynamics of flexible bodies.
16. A. A. Shabana 1986 *Transactions of the ASME Journal of Applied Mechanics* **108**, 358–366. Dynamics of inertia variant flexible systems using experimentally identified parameters.
17. A. A. Shabana 1989 *Dynamics of Multibody Systems*. New York: John Wiley and Sons.
18. A. A. Shabana 1990 *International Journal of Non-linear Mechanics* **25**, 153–162. On the use of finite element method and classical approximation techniques in the non-linear dynamics of multibody systems.
19. A. A. Shabana 1990 *Transactions of the American Society of Mechanical Engineers*, *Journal of Applied Mechanics* **112**, 496–503. Dynamics of flexible bodies using generalized Newton–Euler equations.
20. A. A. Shabana 1991 *International Journal of Numerical Methods in Engineering* **32**, 1813–1831. Constrained motion of deformable bodies.
21. A. Leissa 1993 *Vibrations of Plates*. Acoustical Society of America.
22. Yu and C. D. Mote, Jr. 1987 *Journal of Sound and Vibration* **119**, 409–427. Vibration and parametric excitation in asymmetric circular plates under moving loads.
23. H. Vinayak and R. Singh 1996 *Journal of Sound and Vibration* **192**, 741–769. Eigensolutions of annular-like elastic disks with intentionally removed or added material.
24. H. Vinayak and R. Singh 1994 *Proceedings of International Gearing Conference*, *Newcastle upon Tyne*, 105–110. Dynamic analysis of flexible gears for high power density transmissions.
25. J. L. Lin and W. Soedel 1988 *Journal of Sound and Vibration* **122**, 547–570. On general in-plane vibrations of rotating thick and thin rings.
26. J. L. Lin and W. Soedel 1988 *Journal of Sound and Vibration* **121**, 317–337. Dynamic response of a rotating, thick ring to force or displacement excitation.
27. W. Soedel 1993 *Theory of Plates and Shells*. New York: Marcel Dekker.
28. S. C. Huang and W. Soedel 1987 *Journal of Sound and Vibration* **118**, 253–270. Response of rotating rings to harmonic and periodic loading and comparison with the inverted problem.

29. S. C. Huang and W. Soedel 1987 *Journal of Sound and Vibration* **115**, 253–27?. Effects of coriolis acceleration on the free and forced in-plane vibrations of rotating rings on elastic foundation.
30. S. C. Huang and W. Soedel 1988 *Journal of Sound and Vibration* **55**, 231–233. Effects of coriolis acceleration on the forced vibration of rotating cylindrical shells.
31. *Load Distribution Program* (*LDP* 8.2) 1993. Gear Dynamics and Gear Noise Research Laboratory, The Ohio State University.
32. R. D. Mindlin and H. Dereshowitz 1954 *Journal of Applied Physics* **25**, 1329–1332. Thickness-shear and flexural vibrations of a circular disk.
33. I. Hayashi, N. Iwatsuki and H. Maki 1994 *Journal of Sound and Vibration* **173**, 633–655. The theoretical modal analysis of a circular plate with a solid shaft.
34. I. Hayashi, N. Iwatsuki and H. Maki 1994 *Journal of Sound and Vibration* **173**, 657–682. The estimation and measurement of the sound power radiated from a circular plate with a solid shaft subjected to an axial load.
35. *ANSYS*, version 5.0, 1993. Swanson Analysis Systems Inc., Houston, PA.
36. R. D. Mindlin 1951 *Transactions of American Society of Mechanical Engineers*, *Journal of Applied Mechanics* **18**, 31–38. Influence of rotatory inertia and shear on flexural motions of isotropic elastic plates.
37. B. Singh and S. Chakarverty 1994 *Journal of Sound and Vibration* **173**, 289–299. Use of characteristic orthogonal polynomials in two dimensions for transverse vibration of elliptic and circular plates with variable thickness.
38. G. W. Blankenship and R. Singh 1995 *Mechanism and Machine Theory* **30**, 323–339. Force transmissibility in helical gear pairs.
39. A. Kahraman and R. Singh 1991 *Journal of Sound and Vibration* **146**, 153–156. Interactions between time-varying mesh stiffness and clearance non-linearities in a geared system.
40. P. Nogill 1987 *Ph.D. Dissertation*, *North Carolina State University*. An analytical investigation of geared system dynamics containing spur and helical gears.

APPENDIX: LIST OF SYMBOLS

$\mathbf{A}$	rotational transformation matrix
A	accelerance
$\mathbf{a}$	acceleration of point P on gear i
$\hat{\mathbf{a}}, \hat{\mathbf{b}}, \hat{\mathbf{c}}, \hat{\mathbf{d}}, \hat{\mathbf{e}}$	Fourier coefficient vectors
a, b	shaft lengths
$\mathbf{C}$	damping matrix
CS	trignometrical shape functions
c_d	damping proportionality constant
$\mathbf{D}$	differential operator matrix
$\mathbf{E}$	elasticity matrix
E	Young's modulus
$\mathbf{F}$	force vector
$\mathbf{F}$	discrete Fourier transform (DFT) matrices
f	frequency (Hz)
f_n	natural frequency (Hz)
f_r	natural frequencies
$\mathbf{G}$	Euler parameter matrix
g, i, j, k, l, p, q	indices
H	compliance
h	contact line offset
$\mathbf{I}$	identity matrix
i, j	gear number
K	scalar stiffness value
$\mathbf{K}$	stiffness matrix
L	overall rms error in mode shape
$\mathbf{D}$	Fourier differentiation matrix
$\mathbf{M}$	inertia matrix
$\mathbf{m}$	inertia sub-matrices
m	modal index in the radial direction (r)

m, n	harmonic order
m_g	gear speed ratio
N	number of terms, holes or gears
n	modal index in the circumferential direction (θ)
$\hat{\mathbf{n}}$	bearing position vector
$\mathbf{P}$	polynomial shape function
P	a point on the line of contact
p	net transmission error
$\mathbf{Q}$	generalized force vector
$\mathbf{q}$	generalized coordinate vector
R	subspace
$\mathbf{R}$	generalized translational co-ordinate
R	residue
r, θ, z	cylindrical co-ordinate
$\mathbf{r}$	vector position of a point in the geometric co-ordinate
r	radius or modal index
$\bar{r}$	dimensionless radius (r/r_o)
$S, \mathbf{S}$	shape function and shape function matrix
SC	trigonometrical shape function
T	kinetic energy
$\mathbf{T}$	torque vector
t	time
U	potential energy
$\bar{\mathbf{u}}$	vector position of a point in the geometric co-ordinates with respect to the centroid
$\hat{\mathbf{u}}, \hat{\mathbf{v}}, \hat{\mathbf{w}}, \hat{\mathbf{p}}, \hat{\mathbf{q}}$	unit vectors along the mesh coordinates
V	volume
$\mathbf{X}$	state space system variable
X, Y, Z	co-ordinate system
χ, γ, ϕ	mesh co-ordinate system
χ, σ, η	helical mesh coordinate system
δ	mesh displacement (with subscript)
δ	small change (without any subscript)
Φ	mean square norm
ϕ	gear diameter
Γ	contact length
Γ	material removal or addition fraction
η	shape function participation factor
λ	eigenvalue parameter (dimensionless)
μ	mesh space
ν	sub-harmonic index
Θ	damping matrix
Θ	trigonometric shape function
θ	generalized rotational coordinate
θ	nominal angular position
ρ	density
σ	boundary condition
τ	non-dimensionalized time
Ξ	system matrix
Ω	rotational speed (r.p.m. or Hz)
ω	natural frequency (rad/s)
ξ	radius of circular holes
ξ_r	damping ratio of rth mode
ψ	mode shape
$\overline{\psi}$	normalized modal displacement
Ψ	helix angle
ζ	shaft subspace

Superscripts

T	transpose

i, j	gear numbers
ℓ	gear number
p	order of differentiation
*	pseudo
$\langle -1 \rangle$	term by term inverse

Subscripts

f, g, k, l, m, n, p, q	indices
ff	flexibility
G	body co-ordinate system
g	rigid body blank motion
Gm	geometric co-ordinate system
H	material removal (holes, slots, etc.)
i	inner
k	bearing number
m	dynamic
md	dynamic (dissipative)
me	dynamic (elastic)
o	mean
q	generalized co-ordinates
Q	hub
R	linear
s	shaft
sB	shaft bending
sR	shaft rocking
sT	shaft longitudinal
b	bearing
R	rim
ROT	rotational
r	modal index
rms	root mean square
$\mathbf{S}$	shape function
x, y, z	co-ordinates
ϵ	transmission error
θ	angular
σ	linear position along the line of contact
$\tilde{}$	asymmetric matrix

Abbreviations

Expt.	experimental
FEM	finite element method
LTI	linear time-invariant
LTV	linear time varying
MBD	multi-body dynamics
STE	static transmission error
diag	diagonal matrix
vec	vectorize